3-14-2008

An Image Based Bidirectional Reflectivity Distribution Function Experiment

Michael T. Hagg

AN IMAGE BASED BIDIRECTIONAL REFLECTIVITY DISTRIBUTION FUNCTION EXPERIMENT

THESIS

Michael T. Hagg, Captain, USAF
AFIT/GEO/ENP/08-M03

DEPARTMENT OF THE AIR FORCE
AIR UNIVERSITY

AIR FORCE INSTITUTE OF TECHNOLOGY

Wright-Patterson Air Force Base, Ohio

The views expressed in this thesis are those of the author and do not reflect the official policy or position of the United States Air Force, Department of Defense, or the United States Government.

AFIT/GEO/ENP/08-M03

AN IMAGE BASED BIDIRECTIONAL REFLECTIVITY DISTRIBUTION FUNCTION EXPERIMENT

THESIS

Presented to the Faculty

Department of Engineering Physics

Graduate School of Engineering and Management

Air Force Institute of Technology

Air University

Air Education and Training Command

In Partial Fulfillment of the Requirements for the

Degree of Master of Science in Electrical Engineering

Michael T. Hagg, BS

Captain, USAF

March 2008

AFIT/GEO/ENP/08-M03

AN IMAGE BASED BIDIRECTIONAL REFLECTIVITY DISTRIBUTION FUNCTION EXPERIMENT

Michael T. Hagg, BS
Captain, USAF

Approved:

// SIGNED //	14Mar08
Michael A. Marciniak (Chairman)	Date
// SIGNED //	14Mar08
Jack E. McCrae (Member)	Date

Abstract

The temperature dependence of Bidirectional Reflectivity Distribution Functions (BRDFs) is not well documented. For the sake of time and customer demand, current measurements are taken at room temperature, but the reflectivity of a material changes as a function of temperature. The assumption is that this change is uniform, and as such, the BRDF will retain its relative angular shape but perhaps be scaled in magnitude as a function of temperature. When BRDFs are to be used at elevated temperatures, a scaling factor is then applied. In addition, BRDF as a function of rate of change of temperature has been identified by the Directed Energy community as being of interest in optical determination of power on target.

BRDF acquisition is often taken with very expensive pieces of equipment know as gonioreflectometers. The process of collecting a BRDF for a sample can take on the order of a day. To speed the collection of BRDF data, the computer graphics industry developed a technique using a series of images that contain enough information to extract the BRDF of the sample in question.

This experiment begins the journey down the path towards understanding temperature dependence of BRDF through image-based BRDF measurement. With the eventual goal of temperature coupled samples, the size of the optics, used here had to be large to accommodate the size of thermally controlled samples. Much of this initial experimental set up was creating custom components to hold the large optics, the sample or the camera.

Initial data suggests this is a viable approach for BRDF acquisition. Additional calibration and samples with known BRDFs must be used in the future for comparison.

Acknowledgments

First, I would like to thank Dr. Michael Marciniak, my advisor, who suggested this project to me. His guidance and encouragement were greatly appreciated throughout this journey.

Secondly, I would like to thank Mr. Mike Ranft, and Mr. Greg Smith. They went above and beyond to help me find whatever piece of equipment I needed to set up this large experiment.

Next, I would like to thanks Niki Gaber, proprietor of Kava House, for the excellent coffee, and allowing me to spend many hours working on my document at her establishment.

Finally, I would like to thank my family who supported and helped me through the rough patches where nothing seemed to be going right. Without their love and support I would not have made it.

Michael T. Hagg

Table of Contents

Page

Page

Table of Figures

List of Tables

AN IMAGE BASED BIDIRECTIONAL REFLECTIVITY DISTRIBUTION FUNCTION EXPERIMENT

1. Introduction

Bidirectional Reflectivity Distributions Functions (BRDFs) are vital to many aspects of life. Both the military and civilian sectors utilize the BRDF. A BRDF fully describes the reflection of light when it hits a surface. In the civilian sector, BRDF is primarily used in the computer graphics industry (CGI). The effects of increased use of BRDF can be clearly seen when comparing early CGI movies to current CGI efforts. One military application of BRDF information is infrared signature modeling. It can also be applied to determine the power delivered to a target from a Directed Energy weapon. Currently, BRDF information is taken primarily at room temperature. The Optical Measurement Facility (OMF), Materials and Manufacturing Directorate, Air Force Research Laboratory, Wright Patterson AFB, OH, evaluates materials for BRDF, and has the capability to measure at different temperatures, but the work load is based on customer specification. If the customer does not fund temperature dependent measurements, none are taken.

1.1. Problem Statement

Assemble a proof-of-concept experiment for acquiring BRDFs from images. The ultimate goal is to temperature control the sample and acquire BRDF information for several samples at different temperatures.

1.2. Motivation

Image-based BRDF acquisition is much faster than traditional BRDF measurements. In each image is a large range of incident and reflected angles. Essentially each pixel in the image can be considered a BRDF measurement.

1.3. Thesis Overview

This thesis is divided into seven chapters. Chapter 2 introduces or refreshes the reader with the concepts or topics used in developing the rest of this thesis. Chapter 3 discusses the layout of the experiment. Chapter 4 deals with the components that make up the experiment. Chapter's 5 and 6 deal with calibration and data extraction, respectively. Chapter 7 contains the conclusion and recommendations.

This experiment will lead to BRDF acquisition of targets at elevated temperatures. It will enable the Air Force Institute of Technology (AFIT) to measure materials independently. Correlation of room temperature measurements to trusted BRDF data from the OMF or in-house from our own, recently acquired, gonioreflectometer should ensure calibration of this approach.

2. Background

This chapter provides background theory and information about the BRDF. The reader will find this information useful in understanding the experiment described in Chapter 3.

2.1. Radiometry

The study of the transport of electromagnetic radiation is called radiometry. More specifically, radiation transport is typically referred to as being from source to detector. The flux leaving a source per unit area or "exitance," incident on a surface per unit area or "irradiance," or collected by a detector, can all be calculated using radiometry. Table 1 lists five common radiometric quantities, their expressions and units, where dA_s is the differential area of the source, dA_d is the differential area of the detector, $d\Omega_d$ is the differential solid angle subtended by the detector, θ_s is the angle from the observation point to the source surface normal, and Φ_e is the integrated power through the detector. (Dereniak, 1996)

Table 1. Common radiometry quantites

Quantity	Variable	Expression	Units
Radiance	L_e	$\frac{d^2\Phi_e}{dA_s\Omega_d \cos\theta}$	$W \cdot sr^{-1} \cdot m^{-2}$
Intensity	I_e	$\int_{A_s} L_e \cos(\theta_s) dA_s$	$\frac{W}{sr}$
Exitance	M_e	$\int_{\Omega_d} L_e \cos(\theta_s) d\Omega_d$	$\frac{W}{m^2}$
Flux	Φ_e	$\iint_{\Omega_d A_s} L_e \cos(\theta_s)\, dA_s d\Omega_d$	W
Irradiance	E_e	$\frac{\partial \Phi_e}{\partial A_d}$	$\frac{W}{m^2}$

2.2. Bi-Directional Reflectivity Distribution Functions

BRDFs are well known properties of materials. Many papers describe the BRDF, its properties, and models to represent it in gory detail. (Nicodemus, 1977)(Marschner, 2000)(Mukaigawa, Sumino, & Yagi, 2007) This experiment has not progressed to the point that this level of detail is necessary or appropriate; however, general principals of the BRDF will be discussed.

2.2.1. Dimensionality of BRDF

Figure 1 shows the four of five dimensions used here that comprise a BRDF.(Harkiss, 2007) The fifth dimension considered here is wavelength. Other dimensions might be temperature or polarization or orientation of the sample in the case of a non isotropic sample, etc. This experiment uses a monochromatic source for illumination; thus, the wavelength is constant. This effectively reduces the dimensions to two. Only incident and reflected angles will be considered.

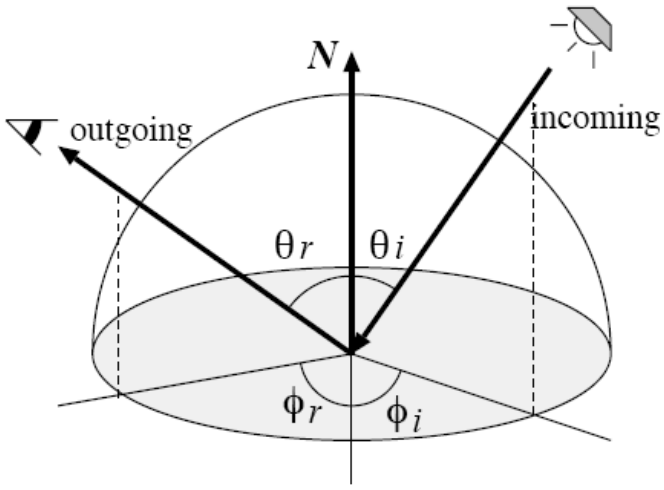

Figure 1. BRDF Geometry

2.2.2. Reciprocity of BRDF

A second principle of a BRDF that allows the function to be useful is reciprocity. Meaning this function can be reversed. The exiting rays from a surface can be reversed and will finish at the source exactly where their source rays started.

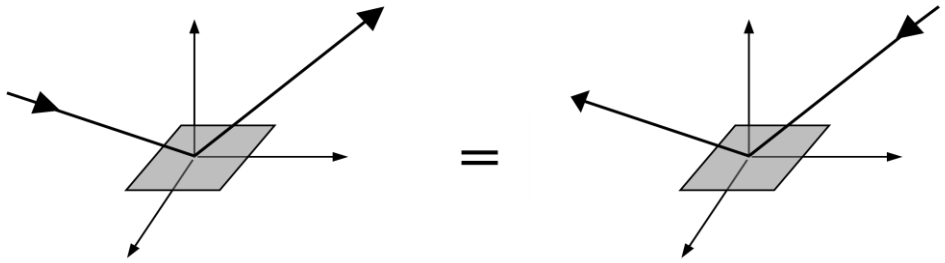

Figure 2. Reciprocity of Reflection

2.2.3. Conservation of Energy

A BRDF must also follow conservation of energy, meaning BRDF must follow equation (1) and must be less than or equal to the amount of incident light applied to the sample.

$$\frac{incidentlight}{incidentlight} = \frac{reflected}{incidentlight} + \frac{absorbed}{incidentlight} + \frac{transmitted}{incidentlight} = 1 \qquad (1)$$

2.3. Background Summary

With some BRDF background now established, Chapter 3 will present techniques for collecting BRDF data.

3. Experiment Layout

This chapter will describe the evolution of the experiment layout. Three major designs were considered before settling on the final. The reasoning behind the change of approach will be discussed. Once the experiment layout is set, the design of each major component will be discussed in Chapter 4.

The computer graphics community is constantly developing new hardware and software to render more realistic graphics. As computer power has increased, the possibility of using BRDF data to improve the realism of rendered scenes became reality. This created a huge demand for BRDF information. In (Marschner, 1999), a technique is presented to quickly acquire BRDF from a series of images.

This work represents an initial attempt at AFIT to develop a workable image-based BRDF acquisition system using collimated laser light and images of a test cylinder or sphere. The ultimate goal will be to take temperature-dependent measurements. As is common with new experiments, many obstacles had to be overcome.

3.1. *Initial Concept*

The initial concept for this experiment is shown below in Figure 3. Illumination of the sample would be accomplished by the central portion of a widely expanded laser beam. The source laser was to be placed 30” above an off-axis parabolic (OAP) mirror. The camera would be fixed in place, and mirrors would change the direction of illumination. The glo-bar was to heat the sample so that temperature-dependent BRDFs could be obtained. The cylindrical sample would be rotated about its center, as shown in the figure. Without this rotation, only “in-plane” measurements are possible from a cylinder. With this rotation, full BRDF measurements are possible.

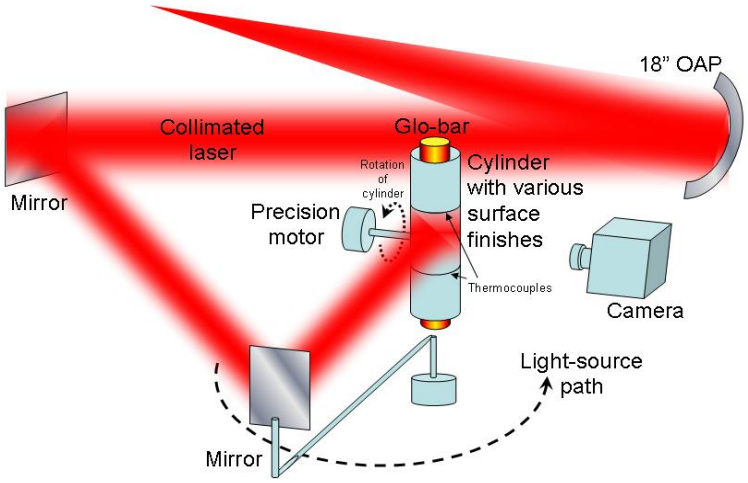

Figure 3. Initial experiment layout

I discovered several issues with this layout. First, it was needlessly complex. Future iterations should be automated to collect data without human intervention. Automation will speed up the data collection process and should increase accuracy by eliminating human error. To automate this setup, precision motors would be needed at each mirror to control their angular rotation. Figure 4 shows the location of motors needed to automate the experiment given this design scheme. Each of these motors would need control schemes built to ensure that the central ray from the first mirror struck the center of the second and then was directed to the center of the sample. The second mirror would also need a motor to rotate the arm. A linear drive would be needed to slide the first mirror along the optic axis of the OAP. This would allow for 180- degree illumination of the sample.

A second issue involves placing the source laser above the OAP. This placement would cause the beam to propagate through eye level before it had expanded to safe intensity. From a laser-safety standpoint, I wanted to avoid having the light propagate through working eye level.

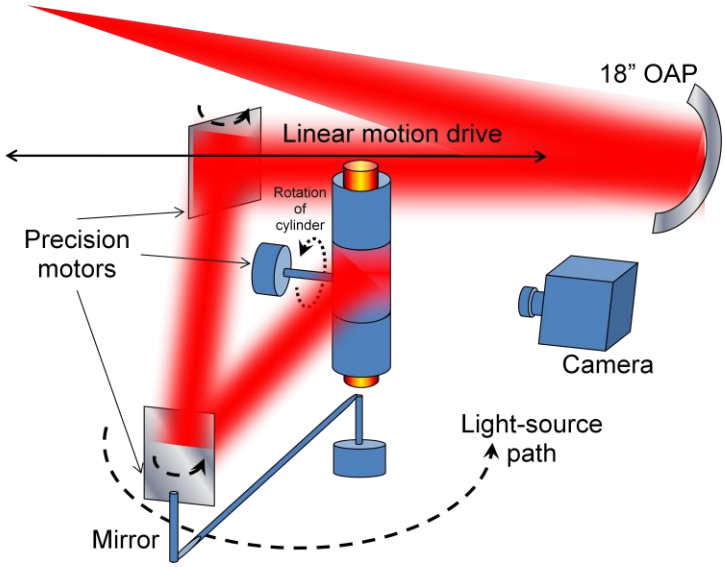

Figure 4. Original concept showing motion requirements

3.2. Intermediate Concept

A much simpler setup would illuminate the sample directly from the OAP and rotate the camera around the cylinder, as shown in Figure 5.

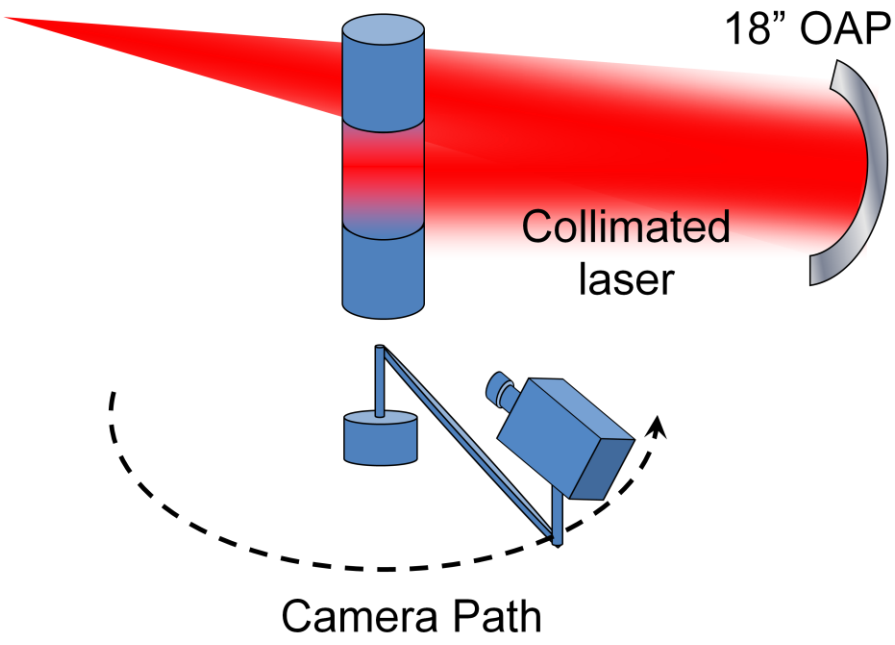

Figure 5. Intermediate experiment set-up

Unfortunately, the quality of the OAP was not good enough to use the collimated laser light for illumination without blurring the pattern the OAP introduces in the beam.

Figure 6(a) shows the optical pattern introduced by the OAP and (b) shows a surface plot produced by L3, the manufacturer of the mirror, showing a very similar error pattern. Appendix E – L3 / Tinsley Mirror Specifications contains information from L3 about the mirror.

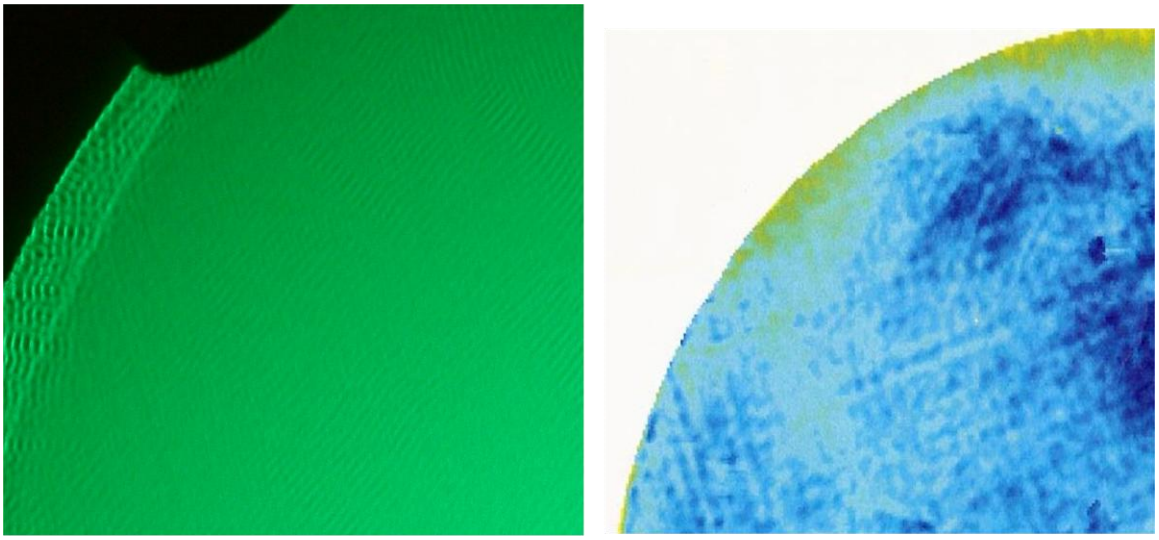

(a) (b)

Figure 6. (a) Reflection from OAP, (b) L3 surface characteristics plot

3.3. Modified Concept

The current layout is shown in Figure 7. This layout is much easier from an automation standpoint than the initial layout discussed above. The only control needed is motor control of the camera mount. Two mirrors are used to direct the beam to the sample. These mirrors were added to reduce the optical pattern introduced into illumination by the OAP. The first turning mirror will be moved across the collimated beam to create a blurring, and thus more uniformly illuminating, effect on the cylinder.

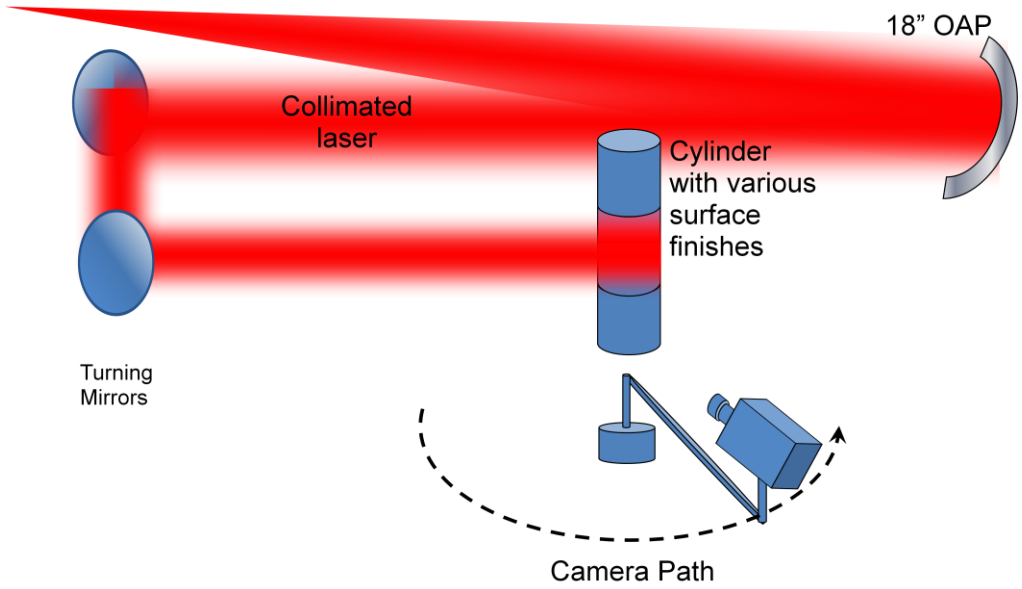

Figure 7. Modified Experiment Layout

3.4. Layout Summary

Now that the experimental layout has been chosen, details of the specific components used will be given in Chapter 4.

4. Experiment Design

This chapter will detail the design of each component of the experiment setup. This experiment was started with two items: the 18" OAP and an air-cooled argon ion laser. The following items needed to be fabricated: a laser mount, turning mirrors, a sample holder, and a camera mount. The laser mount must hold the laser, a beam splitter, an optical power meter, a beam expander, and a spatial filter. The turning mirrors need to be large enough to illuminate the sample when arranged at 45-degree angles to the OAP beam; this turned out to be 8-inch diameter. The camera mount needed to be several feet long to reduce the solid angle from the sample to the camera. In addition, it should support the camera fully with minimal twisting or oscillation forces acting on the camera.

4.1. Laser

The laser available to use for this project was an air-cooled argon ion laser manufactured by Ion Laser Technology, model number 5490 AWC-00C. It has a maximum output power of 50mW at a wavelength of 514nm.

4.2. Off Axis Parabolic Mirror

The OAP, shown in Figure 8, was procured from SSG Tinsley, a L3 Communications subsidiary. The mirror is made from mirror grade Zerodur. It has an aluminum reflective surface and is coated with a protective layer. The key design consideration is the location of the focal spot. The focal spot for this mirror is 30" off center in direction of the vertex and 144" from the center of the mirror in the propagation direction. Equation (2) describes the parabola of the mirror where R is the radius of curvature of the vertex (R = 288" ±1"), K is the conic constant (K = -1), Y is the height from the optical axis.

$$Z = \frac{\frac{Y^2}{R}}{1+\sqrt{1-(K+1)\left(\frac{Y^2}{R^2}\right)}} \tag{2}$$

Figure 8. 18" Off Axis Parabolic mirror

This mirror introduced significant optical artifacts into the collimated beam as was previously shown in Figure 6. The polishing process left surface irregularities on the order of 13λ in the OAP, as shown in Appendix E – L3 / Tinsley Mirror Specifications.

4.3. Laser Mount

With a 144" focal length, the mirror was going to dictate a laser mount that was separate from the optical table. The AFIT machine shop fabricated a mount from 0.25" aluminum plate. Steel would have been preferred, with the added benefit of being able to use magnetic mounts, but 0.25" steel plate was not available at the time of fabrication. Holes were drilled to match the argon-ion laser mount holes, and along the beam exit side of the plate to allow for mounting of additional optical components.

Figure 9 shows the relative position of the laser, turning mirror, aperture, 40x objective lens, 10µm spatial filter, and silicon photodiode. Table 2 shows the manufacturer and model number if available for each component on or connected to the laser mount.

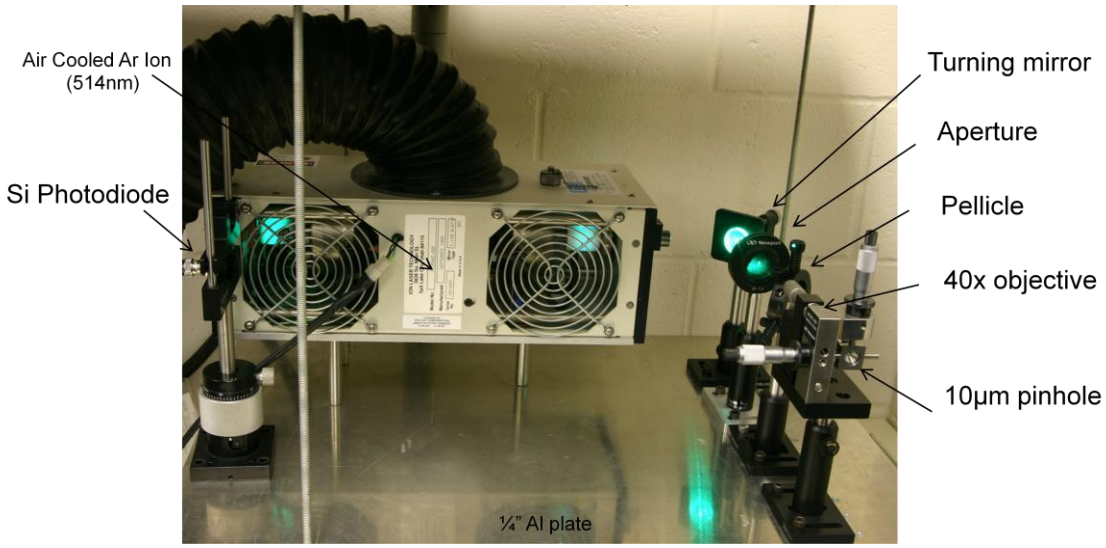

Figure 9. Laser mount layout

Table 2. Component list for Laser Mount

Component	Manufacturer	Model
512nm Ar+ Air Cooled Laser	Ion Laser Technology	5490 AWC-00C
Turning Mirror	Newport	N/A
1" Adjustable Diaphragm	Newport	N/A
Pellicle Beam Splitter	Edmund Optical	39478
Spatial Filter	Newport	900
Silicon Photo Diode	Edmund Optical	53379
Photodiode Amplifier	Terahertz Tech Inc	PDA-750

I chose to use a turning mirror to increase flexibility of placing the optical table and laser mount. Without the turning mirror, alignment was going to be more difficult for two reasons. First, the entire laser mount would need to be moved even for small adjustments. Secondly, with the laser being 18" long, precious space would be wasted in

the axis of the OAP's focal length. The increased length of the laser mount would require the optical table to be moved against the wall of the laboratory. The pellicle beam splitter was added to feed into a silicon photodiode and amplifier. Laser output must be constant while measurements are taken and the beamsplitter/photodiode combination allows the laser output to be monitored. The first aperture was added to reduce scatter from being fed back into the laser and photodiode. A second aperture was added after expansion to limit the light to just striking the OAP. This reduces the retroreflections from the walls of the room and the optical table itself. Before measurements were taken, I surrounded the laser mount with black foam board to reduce reflections from reaching the sample.

4.4. Turning Mirrors

As discussed in Chapter 3, it was necessary to use two mirrors to illuminate the sample. The first mirror will be arranged at a 45-degree angle to the beam and moved in an attempt to illuminate the sample more uniformly. As mentioned before, these mirrors need to be approximately 8" in order to illuminate the 3" diameter aluminum cylinder sample. Commercial optical quality solutions were very expensive at that size, so other options were explored. These options included: standard front silvered mirrors, which were procured from a local glass supply company; 99.999% pure nickel compact disk master blanks; sputtered aluminum on the standard mirrors; and finally, 2500µm thick aluminum sputtered on 0.25" plate glass.

4.4.1. Front Silvered Mirrors

Initial assessment of the front silvered mirrors, shown in Figure 10, was that they were of acceptable quality. This perception changed quickly once they were used to turn

the expanded beam. These mirrors were far too transmissive. In addition, the transmission profile was not uniform, which was the larger problem. The resulting reflections, as shown in Figure 11, were not usable.

Figure 10. Front silvered mirror

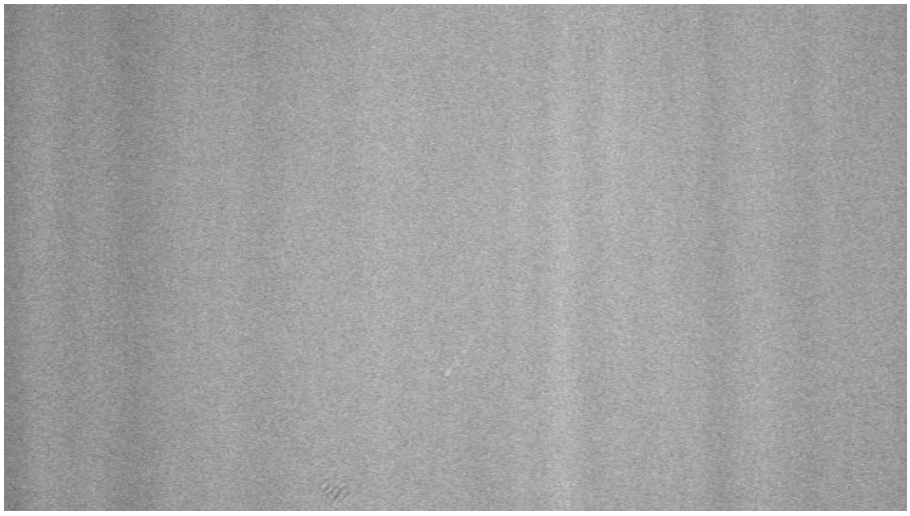

Figure 11. Reflection artifact from Front Silvered Mirror

Transmission information was gathered using a small helium neon (HeNe) laser and Newton optical power meter. The HeNe output power was 3.698mW. Figure 12 shows the transmission of the mirror over a 5cm region. The average transmission over this region was approximately 91µW. A quick calculation reveals transmission of ~2.5%. If the transmission was uniform, this would be an acceptable level of transmission.

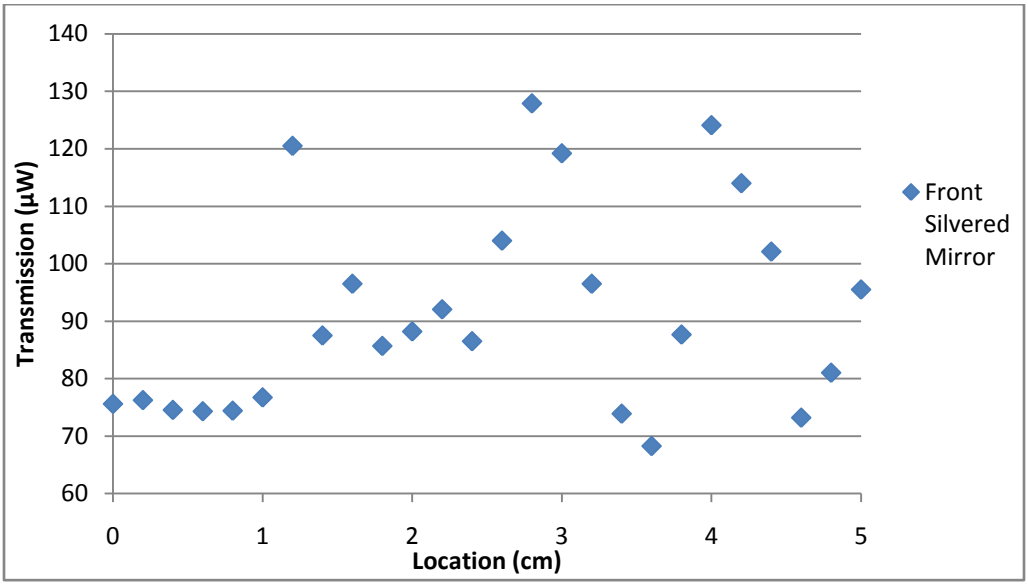

Figure 12. Transmission profile across front silvered mirror

4.4.2. Nickel Mirrors

Three nickel compact disc master blanks were obtained for evaluation as potential turning mirrors. The fabrication process started with a release layer being deposited on a glass substrate. Using vacuum metal deposition, 325 Angstroms of 99.999% nickel was deposited. The remaining nickel was added via electroplating. Final mirror thickness is approximately 10µm. While the nickel mirrors were very smooth and did not transmit light, they were not structurally stable enough to be usable as mirrors. Figure 13 shows a

variation in intensity as well as a distortion of the circular reflection. Even with uniform pressure around the perimeter of the mirror, the reflection was nowhere near good enough for this project. In addition, the reflection from nickel was noticeably dimmer than that of aluminum. Nickel is less reflective at 514nm than aluminum.

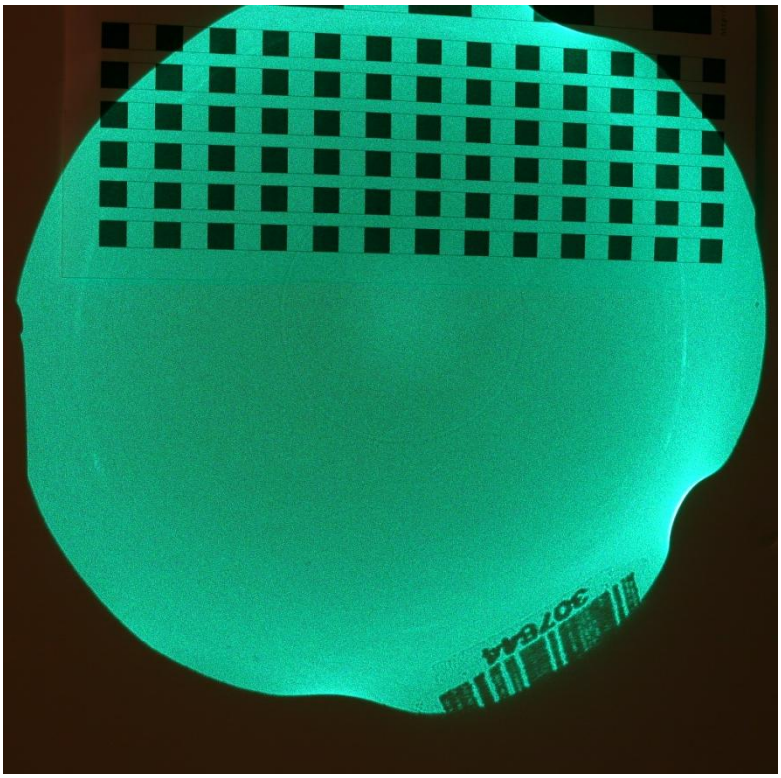

Figure 13. Nickel mirror reflection

4.4.3. *Sputtered Aluminum Mirrors*

The first attempt used one of the 6" square front silvered mirrors discussed above. A layer of aluminum was sputtered directly on top of the surface already silvered. When compared with an original front silvered mirror, transmission was reduced, but the variations shown in Figure 11 were still visible.

Transmission information was gathered exactly as with the front silvered mirror. Figure 14 shows that although the transmission is greatly reduced, to ~0.01%, the underlying non-uniformity problem still exists.

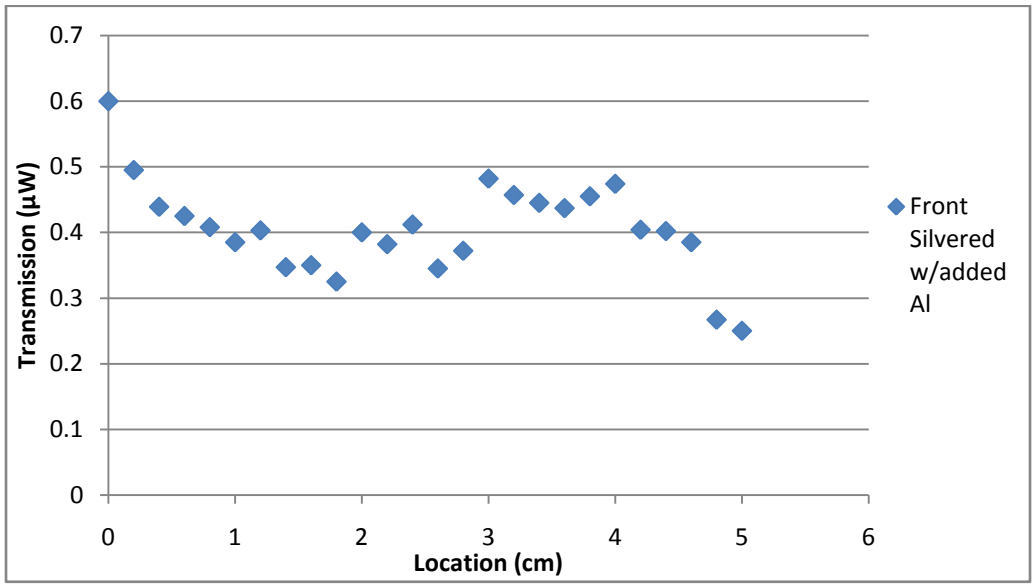

Figure 14. Transmission profile across front silvered mirror with added Al

The second attempt used quarter inch plate glass sourced from and cut by a local glass supplier. They were taken to the AFIT clean room, cleaned with acetone, methanol and isopropyl alcohol. The maximum size our metal vaporizer will hold is 8 inches, and fortunately, that is large enough to cover the test sample. Following cleaning, aluminum was sputtered onto the glass substrate to a thickness of 2500µm.

These mirrors are relatively stable structurally. However, it is still possible to deform them under a stress gradient. To reduce stress on the mirrors, I designed and had the AFIT machine shop fabricate circular mirror mounts. The mounts contain three set screws to distribute pressure on the mirror.

All things considered, these mirrors turned out to be acceptable. The transmission was not measurable. With proper care mounting them, they are acceptably flat and produce reflections with no visible defects.

4.5. Optical Table Set-up

The optical table was set up with the OAP as far back and to the edge as possible. An index system for the holes in the optical table was devised and is shown in Figure 15.

The (x, y) center of the OAP is at (8, 109). Specific use of the index reference will be discussed in the alignment section. The turning mirrors are centered at (28.5, 14.5) and (28.5, 62.5) for turning mirror one and two (TM1, TM2) respectively. The camera mount sample holder is centered at (62.5, 62.5). The complete optical table setup is shown in Figure 16.

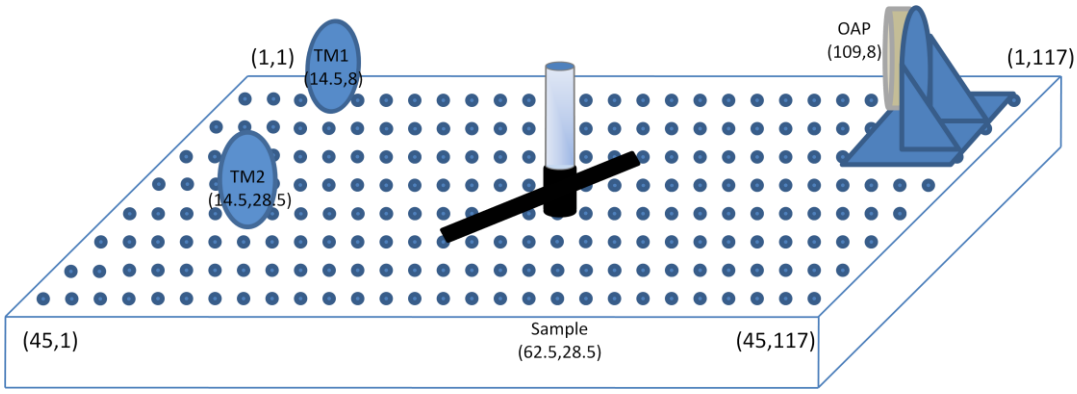

Figure 15. Optical table overview

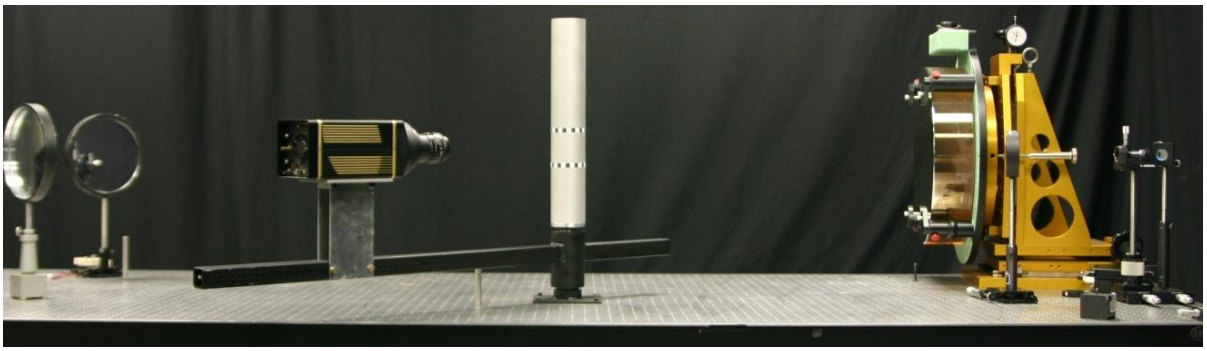

Figure 16. Photograph of optical table setup

4.6. Design Summary

Having chosen the experimental layout in Chapter 3, each component of the experimental set-up was designed here in Chapter 4. The alignment and calibration of these components will now be accomplished in Chapter 5.

5. Alignment and Calibration

This chapter will discuss the initial placement of the laser, methods to fine tune its alignment, and calibration issues involved with this experiment.

5.1. Laser Alignment

The specifications of the OAP dictated that the argon ion laser needed to be placed 144" from its center along, and 30" off, its optical axis. The simplest method to pinpoint this location was to use a second laser to send collimated light on a backward path through the experiment. The point at which the laser focuses is the location of the OAP's focal point. The pinhole of the beam expander should be positioned precisely at this point. A 3mW HeNe laser was used to accomplish this task. An initial test was inconclusive due to the small size of the HeNe beam. A second attempt was made after expanding the beam to approximatly 75mm diameter, the size of the available lens, and collimating. Figure 17 shows the layout of the HeNe alignment beam setup. The relative placement of the HeNe setup can be seen in Figure 16. I have chosen to keep the HeNe in place requiring only to move the sample from the beam path to confirm alignment. With careful alignment of all the components, this should be accurate enough to locate the pinhole within the plus or minus 0.25" tolerance of both the off-axis and z-axis positions.

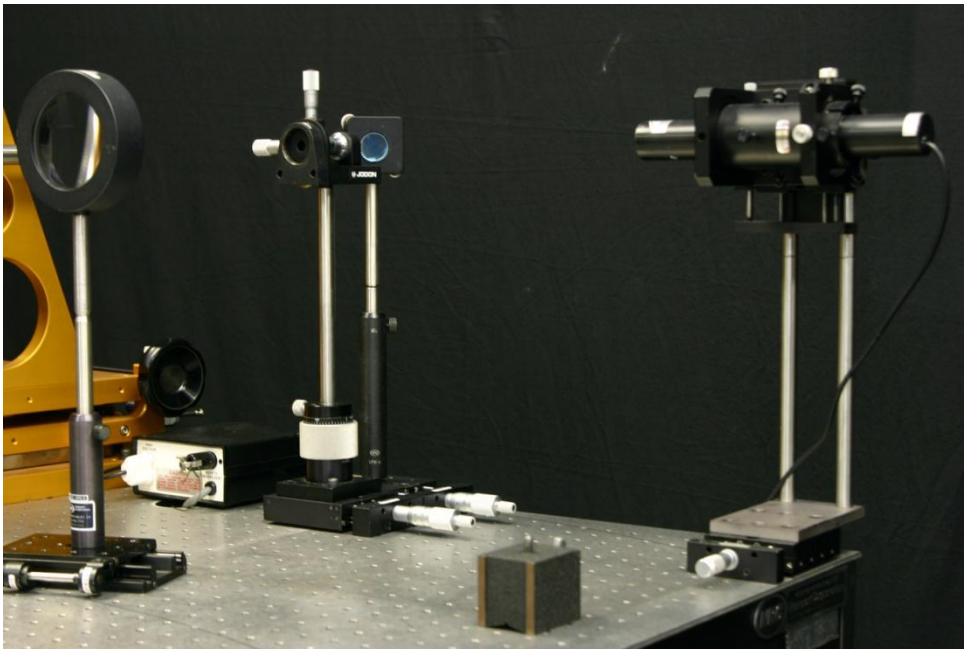

Figure 17. HeNe alignment beam set-up

Once the pinhole is located, the beam must be aligned to the OAP. This turned out to be a relatively easy task. With the laser mount level and at the proper height, the beam can be adjusted with the turning mirror. Of course, the first step was to align the beam to the expanding lens and pinhole. Once this is accomplished, small changes of mirror position and pinhole, in succession, can move the beam to the center of the OAP and keep the higher-order modes out of the expanded beam. To improve alignment, I use an optical power meter placed at the center of the OAP, and continue to adjust the laser mount turning mirror and pinhole until optical power is at a maximum.

The expanded beam size must overfill the OAP. The point of this is to have a beam of uniform intensity to illuminate the test sample. The initial attempt to fill the mirror with a 20x objective lens fell short of filling the mirror. A 40x objective lens was able to expand the beam adequately, but presented a second problem. The beam was now focusing so fast that the 25μm pinhole could not filter the higher order modes out of the

beam. Changing to a 10μm pinhole solved this problem. The beam was now of sufficient diameter and sufficiently single mode to provide illumination for this project.

5.2. Camera Alignment

The camera used for this experiment is a PIMAX camera made by Princeton Electronics. This camera has a 512 by 512 pixel Intensified Charged Coupled Device (ICCD) sensor fiber optically coupled to the lens. The lens used was a 50mm Nikon lens with a maximum aperture of f/1.4. While this lens had a large maximum aperture, it was not appropriate to use it wide open in this experiment. When set to an f/1.4 aperture, the lens has very shallow depth of field. To ensure that the entire sample was in the depth of field, the aperature was stopped down to f/8.0. The downside of stopping the lens down is that integration time must increase as fewer photons per unit time will be striking the sensor. The upside is that this reduces the uncertainty introduced by the solid angle subtended by the camera from the sample.

Camera alignment was accomplished using WinView32 acquisition software. The camera mount, shown in Figure 18, has holes every half inch to allow for different camera and lens combinations. My ideal setup is that the camera's image completely covers the test cylinder and has a small region on each side of the sample that shows the background. I adjusted the camera position until the test sample filled the image satisfactorily. The sample covered 475 of the 512 total pixels across the image. The front of the lens is 32 cm from the center of sample mount.

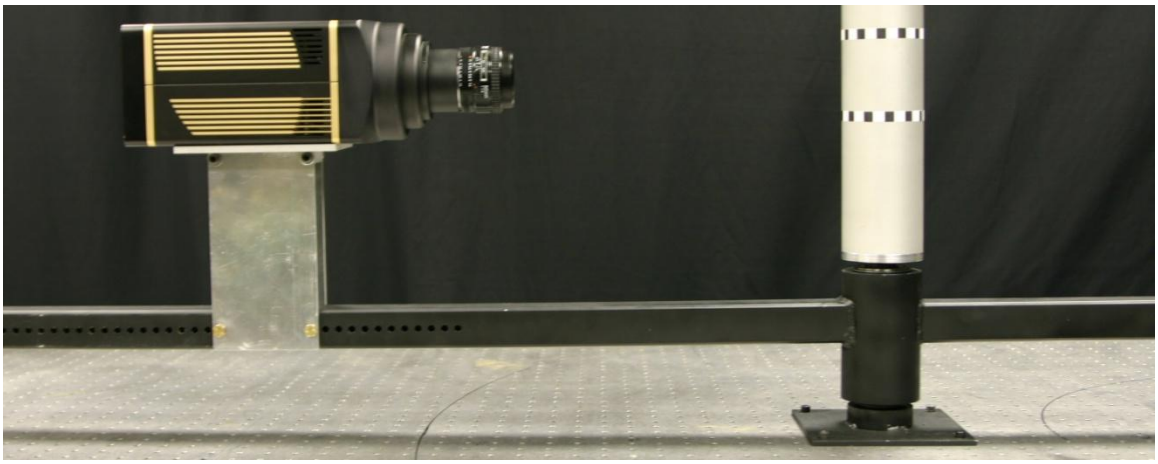

Figure 18. Camera mount

5.3. Geometrical Alignment

The goal of geometrical calibration is to determine the area of the test sample that correlates with each pixel in the detector. The size of the target, the distance from the target to the imaging system, the area of the detector, and the number of pixels all must be known.

Figure 19 shows the relative positions of the cylinder, lens, and detector. Since the surface of the cylinder curves away from the camera towards the edges of the image, there is more surface area covered by pixels near the edges than in the center of the cylinder. The number of pixels covering the cylinder was determined by examining several test image plots and determining the first and last pixel that contains cylinder information. Figure 20 shows the geometry for determining the angle covered.

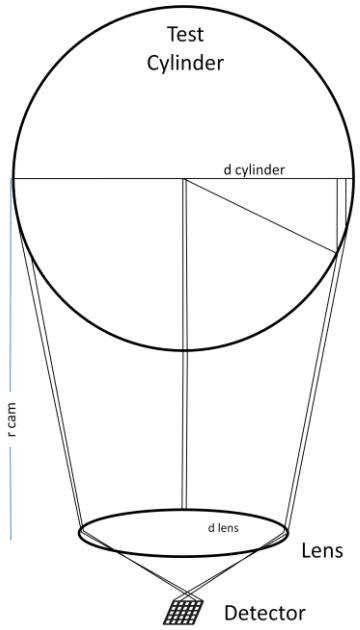

Figure 19. Geometric Alignment

I have determined each pixel covers 160μm (Δpix) along the diameter of the cylinder using Equation (3) and using the d_{cyl}=76.2mm. The angle covered by a pixel is illustrated in Figure 20, and calculated in Equation (4), where $1 \le i \le 475$ and r_{cyl}, the radius of the cylinder, is 38.1mm.

$$\Delta pix = \frac{d_{cyl}}{475\, pixels} = 160\,\mu m \tag{3}$$

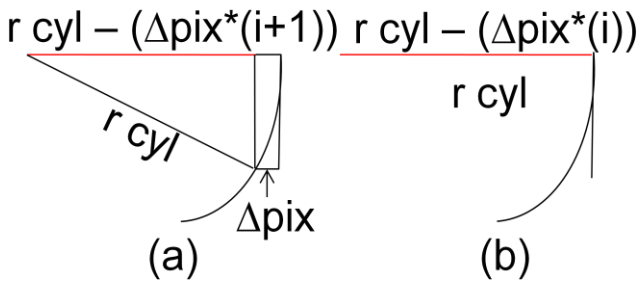

Figure 20. Angle per pixel geometry for (a)previous and (b)current pixels

$$\theta_{pixel}(i) = \cos^{-1}\left(\frac{\left(r_{cyl} - \Delta pix * i\right)}{r_{cyl}} - \frac{\left(r_{cyl} - \Delta pix * \left(i-1\right)\right)}{r_{cyl}}\right) \tag{4}$$

$$\Delta\theta(i) = \frac{\theta_{pixel}(i)}{2} \tag{5}$$

Equation (6) shows the arc length for any pixel, where $\theta_{pixel}(i)$ is found from Equation (4). Equation (7) shows the area of the cylinder covered by a pixel, where h is assumed to be equal to Δpix due to the symmetry of the imaging system.

$$s(i) = \left(\theta_{pixel}(i)\right) r_{cyl} \tag{6}$$

$$Area_{pixel}(i) = s(i) * h \tag{7}$$

Under ideal conditions for BRDF data collection, the area covered by each pixel should be infinitely small. This is not achievable in physical systems. The data that will be presented later should eventually include error bars that will depend on the area covered by the pixel. This will determine a range of incident and reflected angles instead of a discrete angle for the true BRDF. Figure 21 shows the incident angle range each pixel represents. As expected, the pixels at the edges of the image correlate to much more area than those at the center of each image.

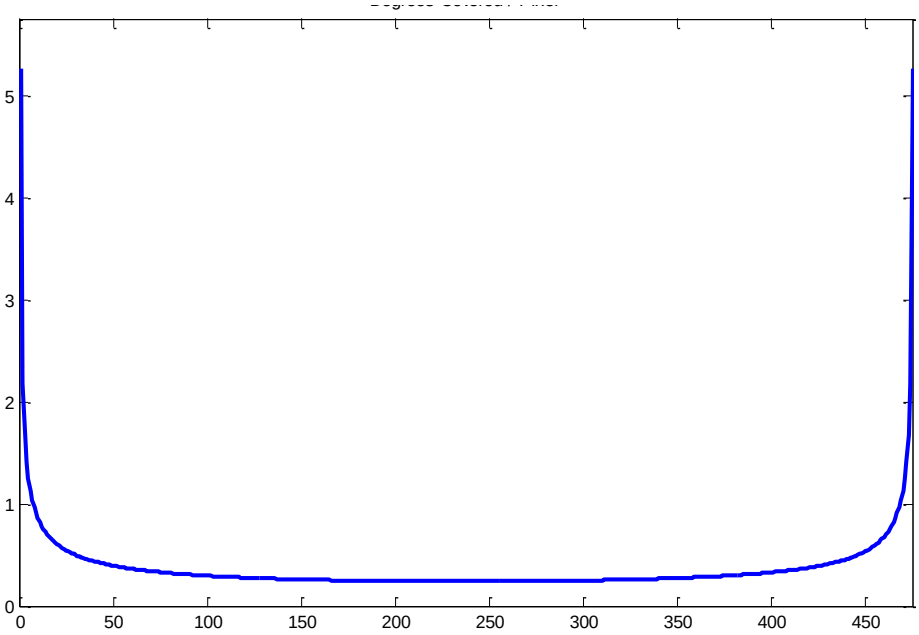

Figure 21. Angular coverage of each pixel

5.4. Radiometric Calibration

To radiometricly calibrate the experiment, several things need to occur. The responsivity of the camera must be accounted for and the camera must be flat fielded. The irradiance of the sample must be fully described and mapped to each incident angle.

My intention when starting this project was to obtain initial results before calibrating the camera to avoid having to duplicate effort, and also to verify the experiment is functioning as intended. Unfortunately, with the delays in the project, time ran out. When it comes time to verify the accuracy of this setup, radiometric calibration will become critical. There is a Matlab toolbox available to make camera calibration easier (Strob, Sepp, Fuchs, Paredes, & Arbeter, 2007).

5.5. Beam Profiles

Following an initial attempt at beam alignment, incident light was measured just before the OAP, TM1, TM2 and the test cylinder. Measurements were made using a 1cm

diameter Newton optical power meter. Figure 22 shows the profile of the expanded beam before the OAP. This beam looks Gaussian as expected. To illustrate the size of the beam, horizontal lines have been included in Figure 22 that represent the size of the OAP and the turning mirrors.

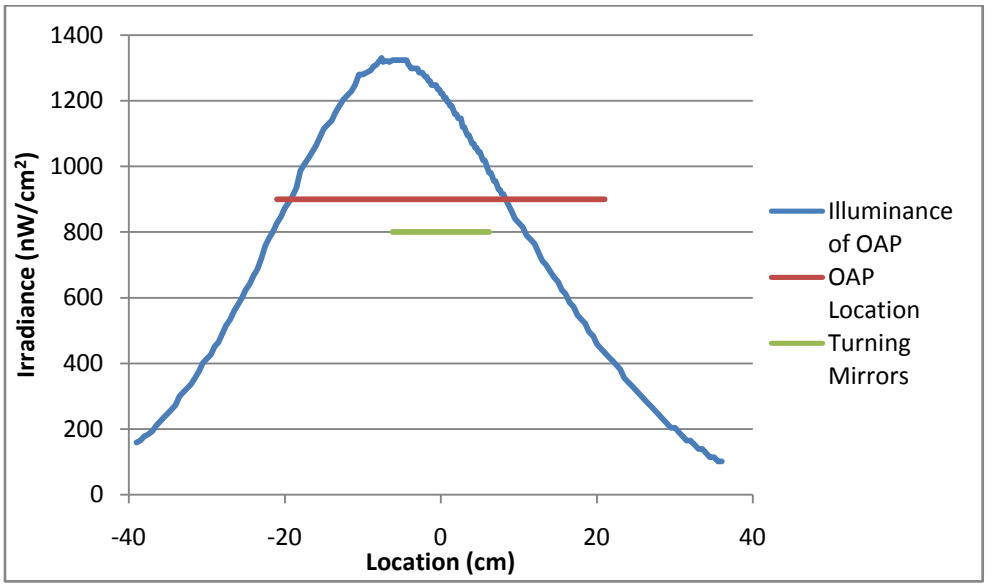

Figure 22. Optical power profile across beam before OAP

Figure 23 is a graph of the optical power profile after the OAP. Primary points of interest are the lack of smoothness in the graph, and the spikes at the edges of the beam. The roughness can be attributed two sources. First, the laser does not hold its output very well. With one person operating the data collection, a finite amount of time is required to adjust the laser back to the desired output and then make a measurement. Second, the optical pattern shown in Figure 6, though small in spatial extent, may play a part. The two spikes correlate to a beveled edge that is machined into the outer edge of the OAP. The last item is the power reduction. In an attempt to show the roughness in these power measurements, I placed an aperture over the optical power meter. The aperture was stopped down to approximately a 2mm diameter. This greatly reduced the power

measured. The anticipated loss from striking the OAP was about 8% based on documentation from L3, shown in Appendix E – L3 / Tinsley Mirror Specifications. Once the size of the aperture was taken into account and the power reading converted to irradiance, the readings correlated nicely with expected values.

As in Figure 22 an indicator of the size and location of TM1 in the beam is included in Figure 23. This visual correlation makes it easier to see the shapes of the graphs propagate from the larger beams to the progressively smaller beams. The reflections from TM1 and TM2 are shown in Figure 24, and again, an indication is included to indicate the size and location of the sample.

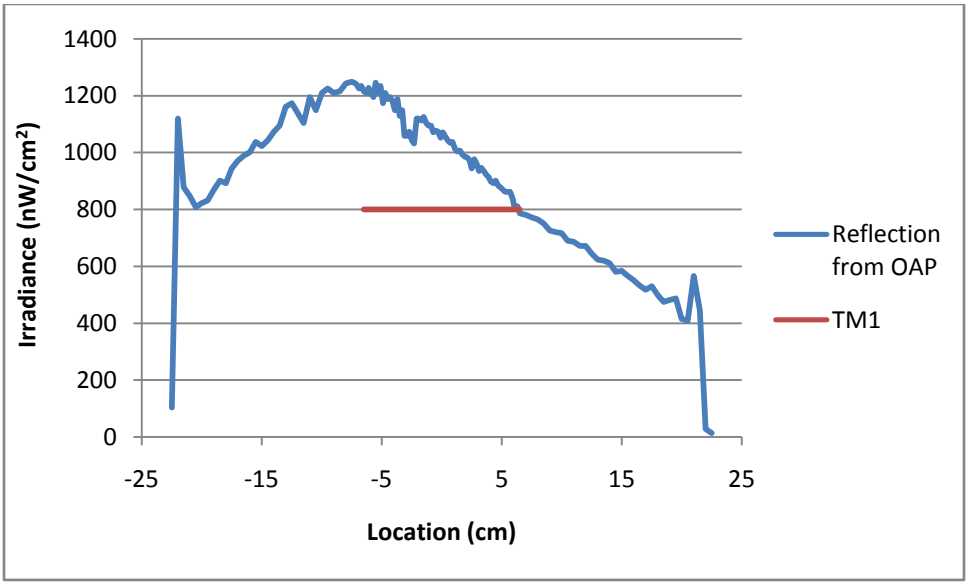

Figure 23. Optical power profile across beam after OAP

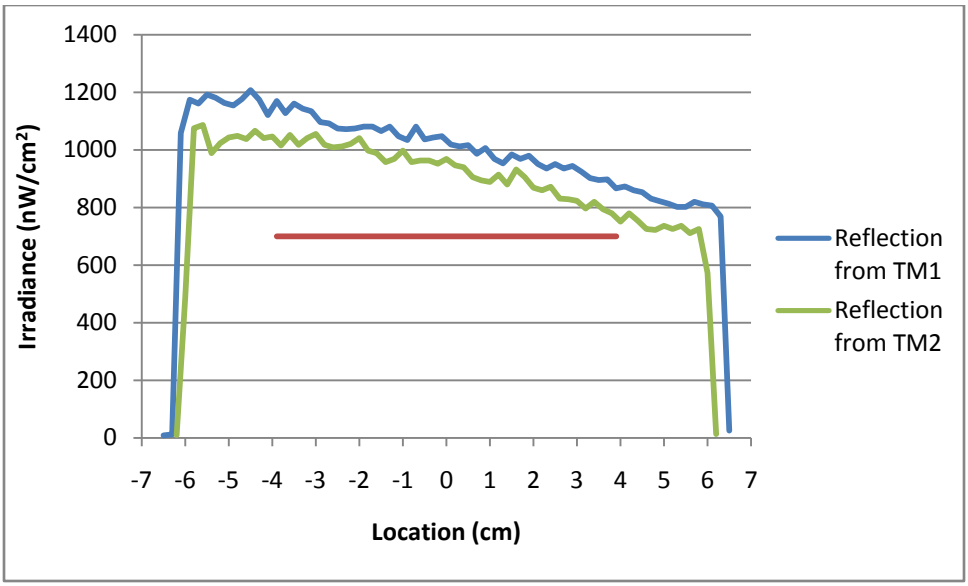

Figure 24. Reflection from Turning Mirrors

Figure 25 shows the profile of the incident laser light on the sample after a second attempt to align the beam. Looking at the profile, it is clear the beam is still not truly aligned. Had it been aligned, a maximum value would be located in the center of the profile. In addition, a profile in the vertical axis should be obtained to properly scale the data. That being said, the power value here does not vary more than ten percent across the profile. With proper alignment, that percentage should come down to much less than five percent. While this is encouraging, the pattern from the OAP was blurred by vibrating TM1. The integration time for the optical power meter is on the order of a fraction of a second. The exposures needed to nearly saturate the camera are on the order of several seconds.

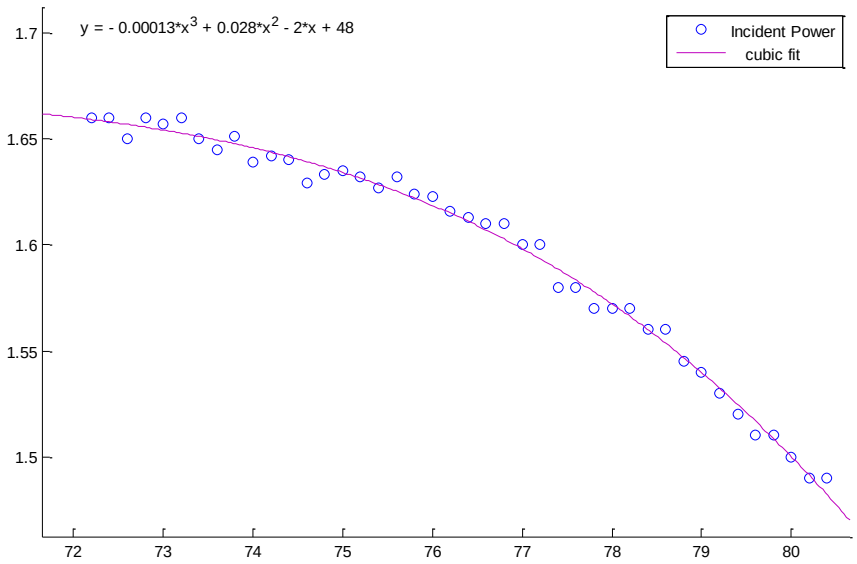

Figure 25. Incident power across sample

In addition, the laser output controller allowed for a fair amount of drift to occur. Over the course of a profile measurement, approximately 30 minutes, multiple adjustments had to be made to keep output within a 0.1mA range. This variability would present a problem when trying to automate collection of samples. A feedback or control loop would need to be created, as well as a correlation between laser output and the power detected by the silicon photodiode.

5.6. Alignment and Calibration Summary

With the shortcomings mentioned in this chapter, no attempt will be made to extract BRDF values from the data collected. However, signal values have been successfully correlated to incident and reflected angles for each pixel. Data extraction from the test image set will be discussed in the next chapter.

6. Data Collection

This chapter will discuss the data set collected that indicates this experiment is viable. The data set and extraction algorithm will be discussed.

6.1. Data Set

The data set I chose to acquire consisted of 11 images. The limited data set was chosen based on a mistaken assumption that additional images would greatly lengthen the data processing time required. Had time remained after discovering the flaw in this reasoning, the data would have included many more images and yielded more populated signal-versus-reflected angle plots.

Signal level is tied to exposure time. For this data set, I chose an exposure time that nearly saturated the camera at a level of $2^{16} = 65,536$. An exposure time of 1.5 seconds accomplished this goal.

Exposure time can also be used to improve the dynamic range of a camera (Robertson, 1999). The series of images in Figure 26 was taken of a diffusely reflecting aluminum cylinder using a common digital SLR CCD camera. Consider the left hand edges of the cylinder and the left-center of the image for the 500-ms and the 8-second exposures. In the 8-second image, a vertical strip appears white in the left-center. In this region, the camera is over saturated. In the same portion of the 500-ms image, there is no saturation and useful information can be gathered. Now consider the left hand edges of the cylinder. The edge cannot be distinguished from the background in the 500-ms image. In the 8-second image, however, the edge is clearly distinguishable. This effect is even more pronounced for objects more specular in nature.

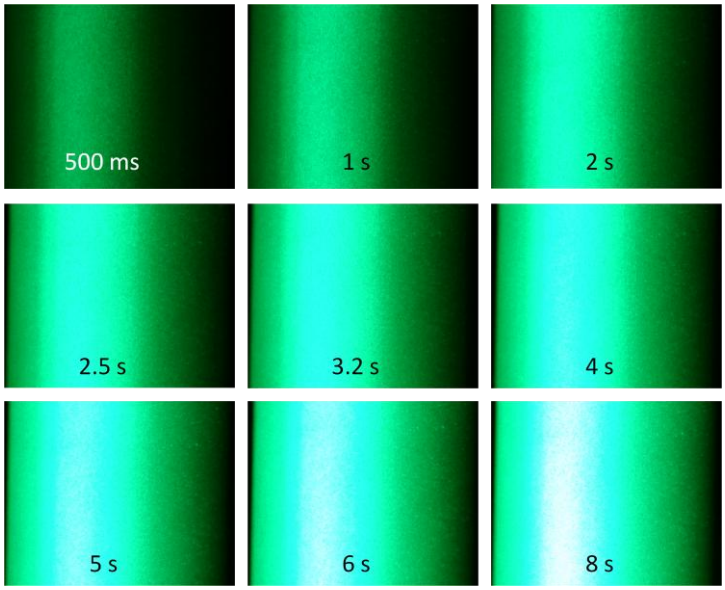

Figure 26. Dynamic range improvement using exposure time

6.2. Data Extraction Algorithm

The purpose of the algorithm is to extract pixel signal values for a given incident angle. The sample is a cylinder and the incident light is collimated, so all incident angles from 0-deg to 90-deg exist twice on the surface covered by the incident beam. Each image then contains, at most, two data points per row of pixels. Figure 27 illustrates this point for a 15-degree camera angle and incident angle of 45 degrees.

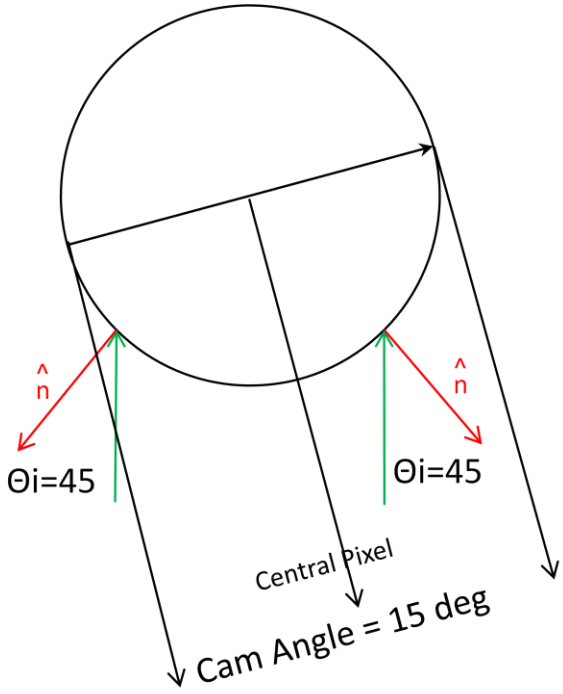

Figure 27. Incident Angles per Image

6.2.1. Camera Angle Calculation

Camera angles were computed to reflect letting the camera mount rest against an optical post screwed into the optical table as depicted in Figure 28. Because of the radius of the optical post (0.26”) and the cross section of the camera arm (0.75”), the geometry was not entirely straight forward for computing the camera angle.

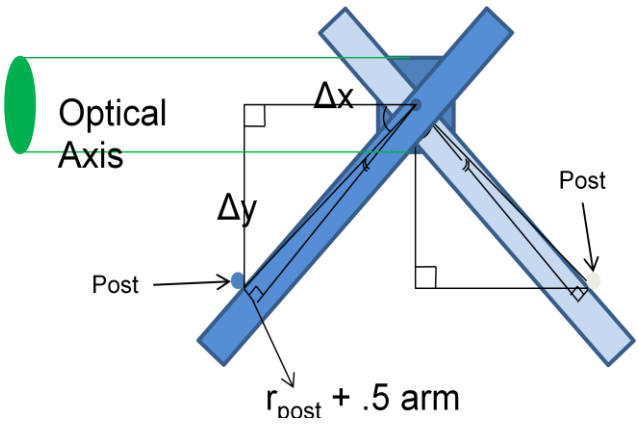

Figure 28. Geometric considerations for camera angle

The camera angle calculation is the sum of two angles. The two angles are the angle from the optical axis to the post (PostAng), and the angle from the edge of the camera arm and the center of the arm (ArmAng). The physical dimensions used are the optical post location, and the sum of the radius of the optical post and half of the camera arm width. Equations (8), (9) and (10) show the calculations required to compute the camera angle, where x and y are locations introduced previously and illustrated in Figure 15.

$$PostDist = \sqrt{\Delta x^2 + \Delta y^2} \tag{8}$$

$$PostAng = \tan^{-1}\left(\frac{\Delta y}{\Delta x}\right) \tag{9}$$

$$ArmAng = \sin^{-1}\frac{\left(r_{post} + \frac{CamArm}{2}\right)}{PostDist} \tag{10}$$

$$CamAng = PostAng + ArmAng \tag{11}$$

A Matlab file was written to calculate the exact camera angle for each viable hole in the optical table. A mount location is available if $|\Delta x| < ArmLength$, and $\Delta y > 0$. The code is included in Appendix A – Camera Angle Code. A table of the angles is included in Appendix C – Camera Angle Table. Table 3 shows the central angle for each image taken for the data set. These values were chosen as the closest available to 15-degree increments starting at 15-degrees. The camera angle will be used in the data extraction algorithm to determine the angle coverage by each pixel.

Table 3. Central rays of test data set

Image	1	2	3	4	5	6	7	8	9	10	11
Deg	15.12	30.02	45.77	60.10	74.96	90.00	105.04	119.90	134.23	149.98	165.00

6.2.2. *Incident Angle Calculation*

The incident angle was calculated for each image. The central ray calculated in the previous section was used as a starting point. The minimum incident angle can be calculated for each image using Equation (12). Calculating the incident angle, θ_{inc}, for each pixel in each image can be done using values calculated earlier. Equation (13) shows the calculation used to determine the central incident angle of each pixel in each image. Figure 29 shows the relation of incident light, surface normal and reflected angles in an image.

$$\theta_{\min}(img) = camang(img) - 90\,\text{deg} \tag{12}$$

$$\theta_{inc}(i, img) = \left(\theta_{\min}(img) + \sum_{n=0}^{i} \theta_{pix}(i)\right) - \Delta\theta(i) \tag{13}$$

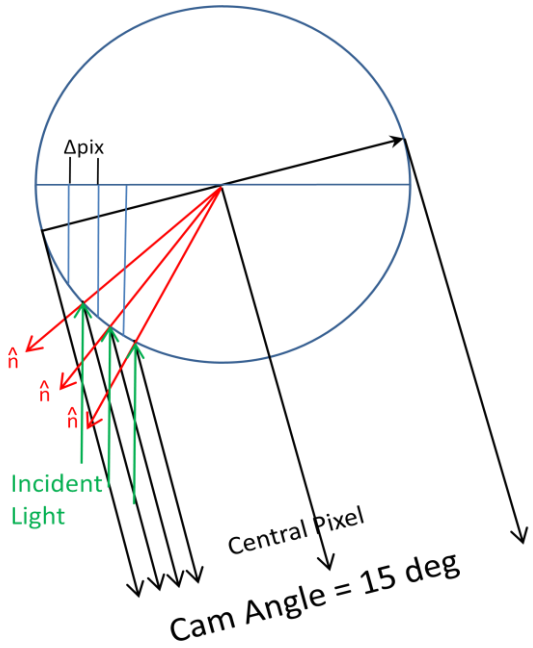

Figure 29. Illustration of Incident Angles

6.2.3. Reflected Angle Calculation

Reflected angles are calculated based on the results of the incident angles calculated in the previous section. The reflected angle is simply an addition or subtraction of the incident angle to the camera angle. Perhaps it is easiest shown with a simple illustration. Figure 30 shows the two reflected angles for a camera angle of 15-degrees. In this specific example, $\theta_{refl\_1} = -45^\circ - 15^\circ = -60^\circ$, and $\theta_{refl\_2} = 45^\circ - 15^\circ = 30^\circ$. In general terms, $\theta_{refl} = \theta_i - \theta_{cam}$, where angles are negative to the camera's left and positive to the camera's right.

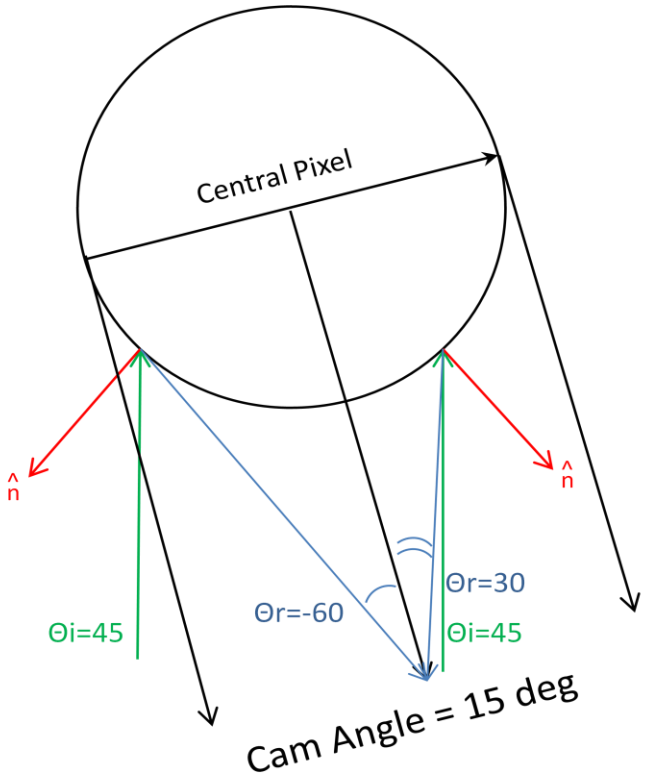

Figure 30. Reflected Angle Illustration

6.3. *Plots*

To demonstrate this is a viable experiment, data must be extracted from the images and compared with similar data. Because the sample was a cylinder, the images contain in-plane data. Figure 31is a composite of three BRDF-versus-reflected angle plots. The test subject was bare aluminum. Figure 32 is a plot of signal versus reflected angle taken from this experiment with a diffuse aluminum cylinder and an arbitrarily chosen incident angle of interest. It contains 11 data points that match the chosen angle of 75 degrees.

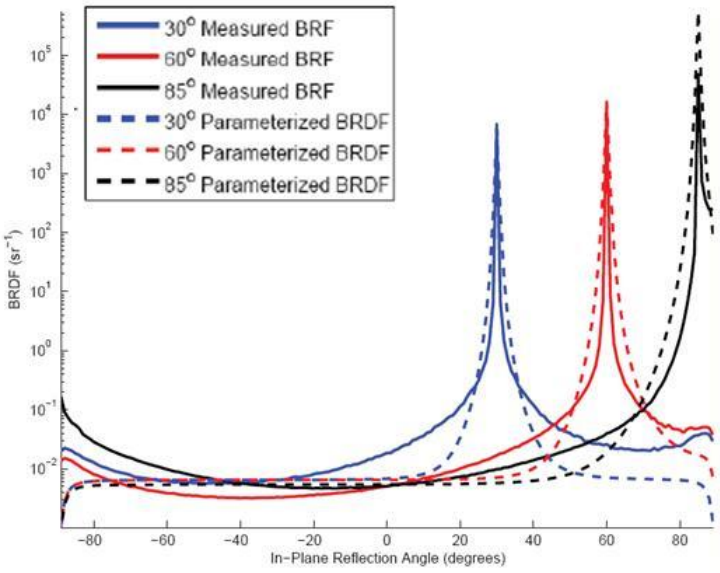

Figure 31. Sample In-Plane BRDF plots (Bortle, 2006)

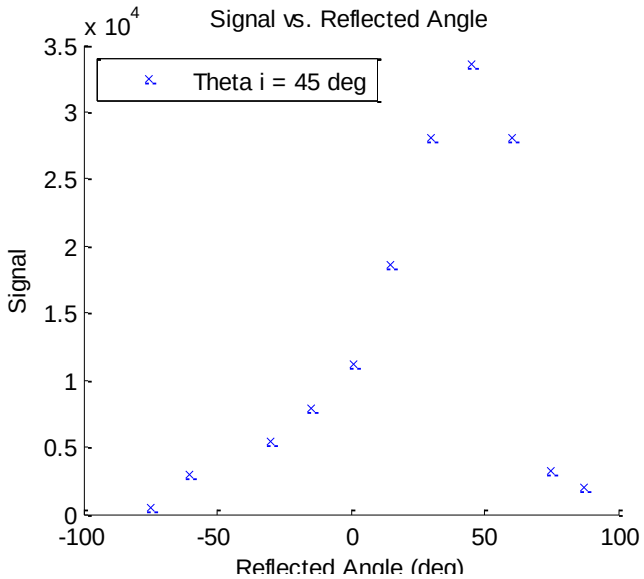

Figure 32. In-Plane signal plot from this experiment

Although this experiment never correlated pixel signal to BRDF, the similarities between Figure 31 and Figure 32 are encouraging. The specular peak occurs around where incident angle = reflected angle. The shape of the plots are similar to one another, though with the data being so sparse it is possible to say it looks like most anything. Looking at a row of image data, there are 475 pieces of signal data. To get more of a hint at the shape of the function it is possible to use a range of incident angles instead of a single angle. Figure 33 shows a series of plots using signal values from pixels located at plus or minus 0, 1, 2, and 3 degrees of the incident angle in question. The only change needed in the data extraction code is an addition of the delta to the incident angle determination criteria.

As delta incident angle is increased, more pixels meet the criteria and are included in the plot. The actual number of pixels represented in Figure 33 are: (a) 11, (b) 46, (c) 104, and (d) 161. Beyond a delta incident of 7.5 degrees, the data starts to overlap and is

badly distorted. This effect can already be seen in Figure 33 (d). The incident angle in question, in this case 45 degrees, is in the middle of each cluster of data points. At the edges of each cluster, the signal is becoming a poorer representation of the actual plot, hence the disagreement between the end of one cluster and the start of the next.

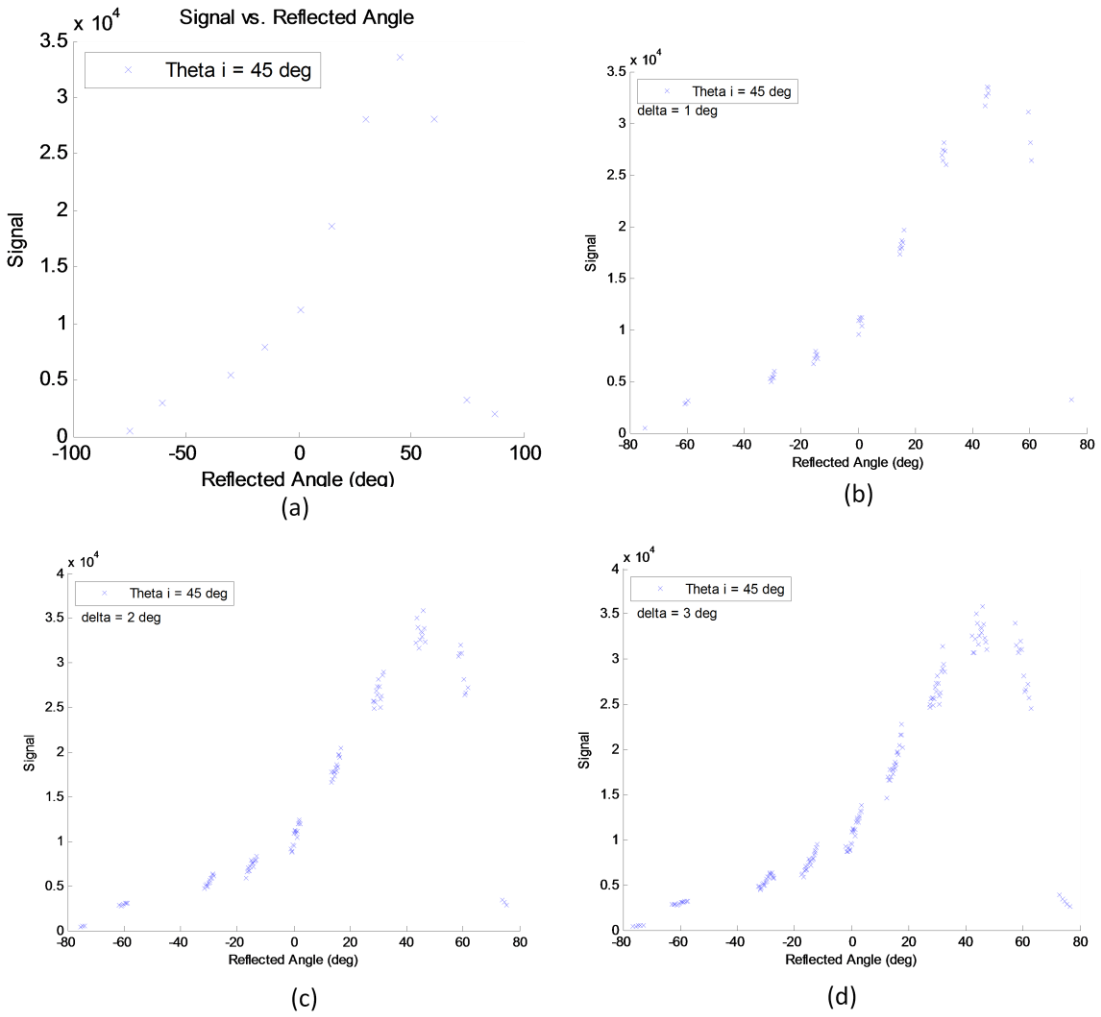

Figure 33. In-Plane signal plots including a range of pixel values clustered around the original (a) Original 11 point plot, (b) delta = 1 deg, (c) delta = 2 deg, (d)delta = 5 deg

6.4. Data Collection Summary

This chapter explained the camera angle, incident angle for each pixel, and reflected angle calculations required to extract signal data from a data image. Signal

versus reflected angle plots were compared to an in-plane BRDF plot. In Chapter 7, conclusions drawn from the experiment to date and recommendations to enhance future iterations will be presented.

7. Conclusions and Recommendations

In this document, a brief background of radiometry and BRDFs, in general, was given. Three different experiment layouts were explored and one was chosen. The design of each component involved in the experiment and obstacles in procuring or fabricating them was discussed. The geometric relationship of each pixel and the cylindrical sample was determined. Calibration issues with this experiment were introduced and the implications they posed were discussed. And finally, data collection and extraction technique was introduced and preliminary results presented.

This project could be characterized by an ultimate triumph over a string of setbacks. The data does behave as expected, but has enough sources of error so as to make BRDF extraction suspect at best. For the next iteration, I would suggest several improvements. Recommendations for each component used are included below.

7.1. Laser mount

The plate was an effective platform. Attaching it to something more stable would be a good idea. Ideally the mount support would attach to the walls or ceiling rafters and be adjustable in the x, y, z and theta directions. This would allow for fine tuning the location of the laser source and would eliminate misalignment from inadvertant bumping into the support stand.

7.2. Off Axis Parabolic Mirror

Ideally, a high quality OAP should be procured to eliminate the pattern that was present in the collimated beam. This would eliminate the need for the turning mirrors as the sample could be illuminated directly.

7.3. Turning Mirrors

The mirrors used turned out better than expected. The biggest improvement could be realized by careful handling of the raw glass during cutting. This would reduce the number of scratches present on the substrate and, in turn, increase the quality of the mirrors. All in all, the sputtered aluminum on plate glass technique produced surprisingly acceptable results.

7.4. Blur Motor

If the OAP cannot be replaced, I would use an active displacement system instead of a passive one. I would tie the mirror mount to a motor via a flywheel device that moves the mount forward and back a set amount, much like a crankshaft and connecting rod drive a piston in an internal combustion engine. The advantage here is that the movement could be quantified as a function of motor rpm.

7.5. Sample

The surface used in this experiment was sandblasted. Since this is a human in the loop process, it is unlikely that the surface is uniform. To improve, I would have the cylinders finished with paint with known BRDF. The paint would have a tendency to fill any small imperfections. Additionally, the paint would allow comparisons with BRDFs taken in the Optical Measurement Facility.

7.6. Thesis Concluding Statement

This experiment was quite a learning experience. I never anticipated the problems I would have during the course of setting up this experiment. In addition, time delays with getting parts custom made added to the adventure.

This experiment gave strong indications that, with some effort to overcome calibration issues, BRDFs can be obtained using this test configuration. Incident-angle-versus- reflected-angle plots looked as they should, so with better accounting of the incident light, and with the recommendations I have made, there is no reason this experiment cannot move forward towards automation and temperature variations of the sample.

Appendix A – Camera Angle Code

```
function [cam_ang] = cam_ang()
%camera mount pivot located at 62.5 , 28.5
x_o = 62.5;
y_o = 28.5;
%Based on length of camera arm "usable" holes are 28,29 to 97,45
X = 28:97;
Y = 29:45;
i=1:68;
j=1:17;
%Pre defining my matrices
post_dist(i,j)=0;
post_ang(i,j)=0;
arm_ang(i,j)=0;
Angs(i,j)=0;
%Need to calculate the angle for each table mount location
j=1;
while (j < 18)
    i=1;
    while (i < 69)
        X(i);
        Y(j);
        delx = X(i)-x_o;
        dely = Y(j)-y_o;

    %We know the distance from the piviot point to the post based on x,y
    %(compute the hyp)
    post_dist(i,j) = sqrt(((delx)^2+(dely)^2));

    %knowing the x,y of the post enables us to find the angle from optic axis
    %to the post
    if (delx<0)
        post_ang(i,j) = deg2rad(90) - atan(abs(delx)/abs(dely));
    else
        post_ang(i,j) =  atan(abs(delx)/abs(dely)) + deg2rad(90);
    end

    %The physical dimentions of the post and camera arm combine for 1 inch
    %from the camera axis.  asin(1/postdist) gives the additional angle
    %angle of the
    arm_ang(i,j) = asin((1.03/post_dist(i,j)));

    %compute the value in degrees
    if delx<0
        Angs(i,j) = rad2deg(post_ang(i,j) + arm_ang(i,j));
    else
        Angs(i,j) = rad2deg(post_ang(i,j) - arm_ang(i,j));
    end
    i = i+1;
    end
    j = j+1;
end
cam_ang = Angs;
```

Appendix B – Signal vs. Reflected Angle Code

```
function [ Data ] = DataExtract(aoi)
%IMPORT will read the images and create a matrix of pixel values for each
%image

base = 'Diff_Cyl_'; % Will need to change for new folders / data runs

IMG(512,512,11)=0;
files = 11;

%angle that the images were obtained from
camangdeg = [15.12, 30.02, 45.77, 60.10, 74.96, 90, 105.04, 119.90, ...
    134.23, 149.98, 165];
camangrad = convang(camangdeg,'deg','rad');

rcyl = 38.1;                %radius of the cylindar in mm
rlens = 26;                 %radius of lens in mm
rcam = 320;                 %radius of the camera arm in mm
numpix = 475;               %number of pixels covering the cylindar
pixinc = (2*rcyl)/numpix;   %incremental distance covered per pixel

%Calculate the angle covered by each pixel and the delta theta of that
%pixel
for i = 1:475
    thetapixrad(i) = acos((rcyl-pixinc*i)/rcyl)-...
        acos((rcyl-(pixinc*(i-1)))/rcyl);
    deltathetarad(i) = thetapixrad(i)/2;
    i = i+1;
end

%Convert calculated values to degrees
thetapixdeg = convang(thetapixrad,'rad','deg');
deltathetadeg = convang(deltathetarad,'rad','deg');

%Index variables
j = 1:512;
k = 1:512;

%Read the image files...
for i = 1:files;
    filename = [base int2str(i)];
    IMG(j,k,i) = csvread([filename '.txt'], 0, 2);
end

%Correct the orientation to reflect experiment setup

for i = 1:files;
    IMG(:,:,i)=IMG(:,:,i)';
end
```

```
%calculate the incident angles covered by each pixel for each image
for i = 1:files
    tot = -90+camangdeg(i);
    for f= 1:475
        tot = tot + thetapixdeg(f);
        theta_i(i,f) = tot-deltathetadeg(f);
    end
end

%Datamining
point = 0;
for i = 1:files
    for f = 1:475
        if ((abs(theta_i(i,f))- deltathetadeg(f) < aoi) && ...
                (abs(theta_i(i,f)) + deltathetadeg(f) > aoi))
            point = point + 1;
            if theta_i(i,f)>0
                ang(point) = camangdeg(i)- (theta_i(i,f));
            else
                ang(point) = -1*(camangdeg(i)- (theta_i(i,f)));
            end
            Data(j,point) = IMG(j,f,i);
        end
    end
end

aoistr = int2str(aoi);
% Create figure
figure1 = figure('Name','Signal Vs Reflected Angle');

% Create axes
axes1 = axes('Parent',figure1,'Position',[0.1169 0.1008 0.775 0.815]);
hold('all');

% Create scatter
scatter (ang, Data(128:256,:),'Marker','x','DisplayName',...
    ['Theta i = ' (aoistr) ' deg'],'Parent',axes1);

% Create xlabel
xlabel({'Reflected Angle (deg)'});

% Create ylabel
ylabel({'Signal'});

% Create title
title('Signal vs. Reflected Angle');

% Create legend
legend1 = legend(axes1,'show');
set(legend1,'Location','Northwest');
for i = 1:10
end

return
```

Appendix C – Camera Angle Table

Y \ X->	30	31	32	33	34	35	36	37	38	39	40	41	42	43	44	45	46	47	48	49
29	2.70	2.78	2.87	2.97	3.08	3.19	3.31	3.44	3.58	3.73	3.90	4.08	4.28	4.50	4.74	5.01	5.31	5.66	6.05	6.49
30	4.46	4.60	4.75	4.91	5.08	5.27	5.46	5.68	5.91	6.16	6.43	6.73	7.06	7.42	7.82	8.26	8.76	9.32	9.96	10.69
31	6.21	6.41	6.61	6.84	7.08	7.33	7.61	7.90	8.22	8.57	8.95	9.36	9.81	10.31	10.86	11.47	12.15	12.92	13.80	14.79
32	7.95	8.20	8.47	8.75	9.06	9.38	9.73	10.11	10.52	10.96	11.43	11.96	12.53	13.16	13.85	14.62	15.48	16.44	17.53	18.77
33	9.68	9.99	10.31	10.65	11.02	11.41	11.83	12.29	12.78	13.31	13.88	14.51	15.19	15.94	16.77	17.69	18.71	19.85	21.13	22.59
34	11.40	11.75	12.13	12.53	12.96	13.41	13.91	14.43	15.00	15.62	16.29	17.01	17.80	18.67	19.62	20.67	21.83	23.13	24.58	26.22
35	13.09	13.49	13.92	14.38	14.87	15.39	15.95	16.54	17.19	17.88	18.63	19.45	20.34	21.31	22.37	23.54	24.83	26.26	27.86	29.65
36	14.76	15.22	15.69	16.20	16.75	17.33	17.95	18.61	19.32	20.09	20.92	21.82	22.80	23.86	25.03	26.30	27.70	29.25	30.97	32.88
37	16.41	16.91	17.44	18.00	18.59	19.23	19.90	20.63	21.41	22.25	23.15	24.12	25.18	26.33	27.58	28.94	30.44	32.08	33.89	35.90
38	18.04	18.58	19.15	19.75	20.40	21.09	21.82	22.60	23.44	24.34	25.31	26.35	27.48	28.70	30.02	31.46	33.03	34.75	36.64	38.71
39	19.63	20.21	20.83	21.48	22.17	22.90	23.69	24.52	25.41	26.37	27.39	28.50	29.68	30.97	32.35	33.86	35.49	37.27	39.21	41.33
40	21.20	21.82	22.47	23.16	23.90	24.67	25.50	26.38	27.33	28.33	29.41	30.56	31.80	33.14	34.58	36.13	37.81	39.63	41.61	43.76
41	22.73	23.39	24.08	24.81	25.58	26.40	27.27	28.19	29.18	30.23	31.35	32.55	33.83	35.21	36.69	38.28	40.00	41.85	43.85	46.01
42	24.23	24.92	25.64	26.41	27.22	28.07	28.98	29.94	30.97	32.05	33.21	34.45	35.77	37.18	38.70	40.32	42.06	43.93	45.93	48.09
43	25.70	26.42	27.17	27.97	28.81	29.70	30.64	31.64	32.69	33.81	35.00	36.27	37.62	39.06	40.60	42.24	44.00	45.87	47.88	50.03
44	27.14	27.88	28.66	29.49	30.36	31.28	32.25	33.27	34.36	35.50	36.72	38.02	39.39	40.85	42.40	44.06	45.82	47.69	49.69	51.82
45	28.54	29.31	30.11	30.97	31.86	32.80	33.80	34.85	35.96	37.13	38.37	39.68	41.07	42.55	44.11	45.77	47.53	49.40	51.38	53.48

Y \ X->	50	51	52	53	54	55	56	57	58	59	60	61	62	63	64	65	66	67	68	69
29	7.01	7.62	8.35	9.23	10.31	11.69	13.49	15.94	19.49	25.07	35.14	59.08	135.00	45.00	120.92	144.86	154.93	160.51	164.06	166.51
30	11.54	12.53	13.70	15.12	16.86	19.05	21.88	25.66	30.98	38.89	51.65	74.05	112.21	67.79	105.95	128.35	141.11	149.02	154.34	158.12
31	15.94	17.29	18.87	20.76	23.07	25.92	29.54	34.26	40.60	49.39	61.94	79.72	102.52	77.48	100.28	118.06	130.61	139.40	145.74	150.46
32	20.19	21.84	23.77	26.06	28.81	32.17	36.32	41.56	48.28	57.01	68.32	82.49	98.81	81.19	97.51	111.68	122.99	131.72	138.44	143.68
33	24.25	26.16	28.37	30.97	34.05	37.73	42.18	47.62	54.31	62.53	72.49	84.11	96.81	83.19	95.89	107.51	117.47	125.69	132.38	137.82
34	28.08	30.19	32.63	35.45	38.74	42.61	47.18	52.61	59.04	66.62	75.37	85.15	95.55	84.45	94.85	104.63	113.38	120.96	127.39	132.82
35	31.67	33.95	36.54	39.51	42.93	46.87	51.43	56.71	62.79	69.72	77.47	85.89	94.69	85.31	94.11	102.53	110.28	117.21	123.29	128.57
36	35.02	37.41	40.12	43.17	46.64	50.57	55.04	60.10	65.80	72.13	79.05	86.43	94.06	85.94	93.57	100.95	107.87	114.20	119.90	124.96
37	38.12	40.60	43.36	46.45	49.92	53.79	58.12	62.93	68.25	74.05	80.29	86.85	93.58	86.42	93.15	99.71	105.95	111.75	117.07	121.88
38	41.00	43.52	46.31	49.40	52.81	56.59	60.75	65.32	70.28	75.61	81.28	87.18	93.20	86.80	92.82	98.73	104.39	109.72	114.68	119.25
39	43.65	46.19	48.98	52.03	55.38	59.04	63.02	67.34	71.97	76.90	82.08	87.44	92.90	87.10	92.56	97.92	103.10	108.03	112.66	116.98
40	46.09	48.63	51.40	54.40	57.66	61.19	65.00	69.07	73.41	77.99	82.76	87.66	92.64	87.36	92.34	97.24	102.01	106.59	110.93	115.00
41	48.34	50.86	53.59	56.53	59.69	63.09	66.72	70.58	74.65	78.91	83.32	87.85	92.43	87.57	92.15	96.68	101.09	105.35	109.42	113.28
42	50.41	52.90	55.58	58.44	61.51	64.77	68.23	71.89	75.72	79.70	83.81	88.01	92.25	87.75	91.99	96.19	100.30	104.28	108.11	111.77
43	52.32	54.77	57.39	60.17	63.13	66.27	69.57	73.04	76.65	80.39	84.23	88.15	92.10	87.90	91.85	95.77	99.61	103.35	106.96	110.43
44	54.08	56.49	59.04	61.74	64.60	67.61	70.76	74.05	77.47	80.99	84.60	88.26	91.96	88.04	91.74	95.40	99.01	102.53	105.95	109.24
45	55.71	58.06	60.55	63.17	65.93	68.81	71.83	74.96	78.20	81.52	84.92	88.37	91.84	88.16	91.63	95.08	98.48	101.80	105.04	108.17

Y \ X->	70	71	72	73	74	75	76	77	78	79	80	81	82	83	84	85	86	87	88	89
29	168.31	169.69	170.77	171.65	172.38	172.99	173.51	173.95	174.34	174.69	174.99	175.26	175.50	175.72	175.92	176.10	176.27	176.42	176.56	176.69
30	160.95	163.14	164.88	166.30	167.47	168.46	169.31	170.04	170.68	171.24	171.74	172.18	172.58	172.94	173.27	173.57	173.84	174.09	174.32	174.54
31	154.08	156.93	159.24	161.13	162.71	164.06	165.21	166.20	167.08	167.85	168.53	169.14	169.69	170.19	170.64	171.05	171.43	171.78	172.10	172.39
32	147.83	151.19	153.94	156.23	158.16	159.81	161.23	162.47	163.56	164.52	165.38	166.15	166.84	167.47	168.04	168.57	169.04	169.48	169.89	170.27
33	142.27	145.95	149.03	151.63	153.85	155.75	157.41	158.87	160.15	161.29	162.31	163.23	164.06	164.81	165.49	166.12	166.69	167.22	167.71	168.17
34	137.39	141.26	144.55	147.37	149.81	151.93	153.78	155.42	156.87	158.17	159.33	160.38	161.33	162.20	162.99	163.72	164.38	165.00	165.57	166.09
35	133.13	137.07	140.49	143.46	146.05	148.33	150.35	152.14	153.74	155.17	156.46	157.63	158.69	159.66	160.55	161.37	162.12	162.81	163.46	164.06
36	129.43	133.36	136.83	139.88	142.59	144.98	147.12	149.03	150.75	152.30	153.70	154.97	156.14	157.20	158.18	159.08	159.91	160.68	161.39	162.05
37	126.21	130.08	133.55	136.64	139.40	141.88	144.10	146.11	147.92	149.56	151.06	152.42	153.67	154.82	155.88	156.85	157.75	158.59	159.37	160.10
38	123.41	127.19	130.60	133.69	136.48	139.00	141.29	143.36	145.25	146.97	148.54	149.98	151.30	152.52	153.65	154.69	155.66	156.56	157.40	158.18
39	120.96	124.62	127.97	131.02	133.81	136.35	138.67	140.79	142.73	144.51	146.14	147.65	149.03	150.32	151.50	152.61	153.63	154.59	155.48	156.31
40	118.81	122.34	125.60	128.61	131.37	133.91	136.24	138.39	140.37	142.19	143.87	145.42	146.86	148.20	149.44	150.59	151.67	152.67	153.62	154.50
41	116.91	120.31	123.47	126.41	129.14	131.66	133.99	136.15	138.15	140.00	141.72	143.31	144.79	146.17	147.45	148.65	149.77	150.82	151.81	152.73
42	115.23	118.49	121.56	124.42	127.10	129.59	131.91	134.07	136.07	137.94	139.68	141.30	142.82	144.23	145.55	146.79	147.95	149.03	150.06	151.02
43	113.73	116.87	119.83	122.61	125.23	127.68	129.97	132.12	134.13	136.00	137.76	139.40	140.94	142.38	143.73	145.00	146.19	147.31	148.36	149.36
44	112.39	115.40	118.26	120.96	123.51	125.92	128.18	130.31	132.31	134.18	135.94	137.60	139.15	140.61	141.98	143.28	144.50	145.64	146.73	147.75
45	111.19	114.07	116.83	119.45	121.94	124.29	126.52	128.62	130.60	132.47	134.23	135.89	137.45	138.93	140.32	141.63	142.87	144.04	145.15	146.20

Y \ X->	90	91	92	93	94	95
29	176.81	176.92	177.03	177.13	177.22	177.30
30	174.73	174.92	175.09	175.25	175.40	175.54
31	172.67	172.92	173.16	173.39	173.59	173.79
32	170.62	170.94	171.25	171.53	171.80	172.05
33	168.59	168.98	169.35	169.69	170.01	170.32
34	166.59	167.04	167.47	167.87	168.25	168.60
35	164.61	165.13	165.62	166.08	166.51	166.91
36	162.67	163.25	163.80	164.31	164.78	165.24
37	160.77	161.41	162.00	162.56	163.09	163.59
38	158.91	159.60	160.25	160.85	161.42	161.96
39	157.10	157.83	158.52	159.17	159.79	160.37
40	155.33	156.10	156.84	157.53	158.18	158.80
41	153.60	154.42	155.19	155.92	156.61	157.27
42	151.93	152.78	153.59	154.36	155.08	155.77
43	150.30	151.19	152.03	152.83	153.58	154.30
44	148.72	149.64	150.51	151.34	152.12	152.86
45	147.20	148.14	149.03	149.89	150.69	151.46

Appendix D – Signal vs. Reflected Angle Plots

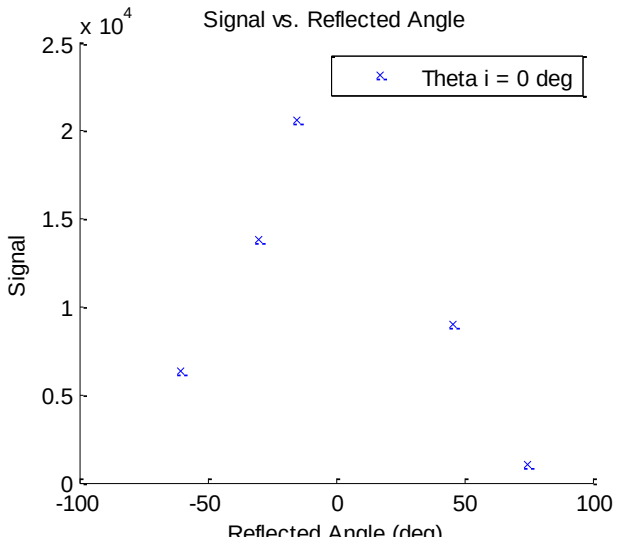

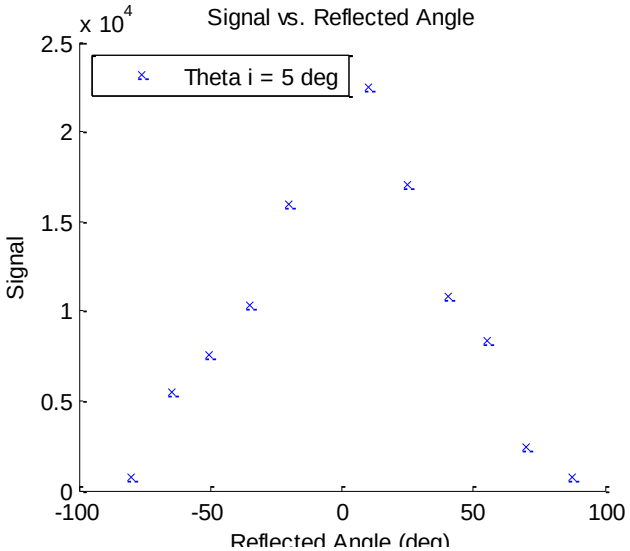

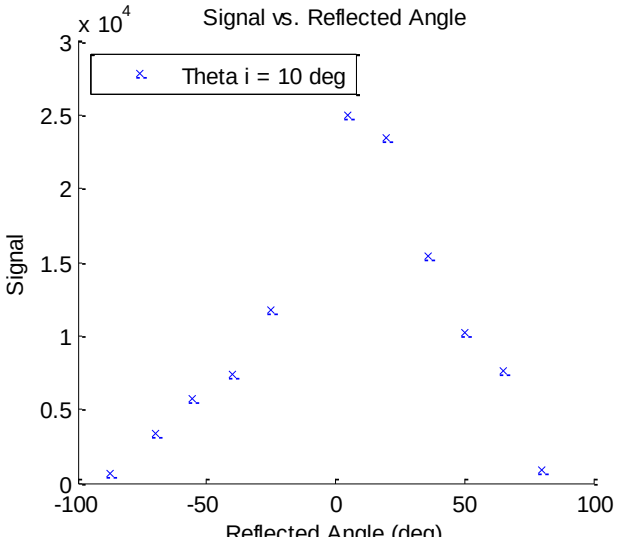

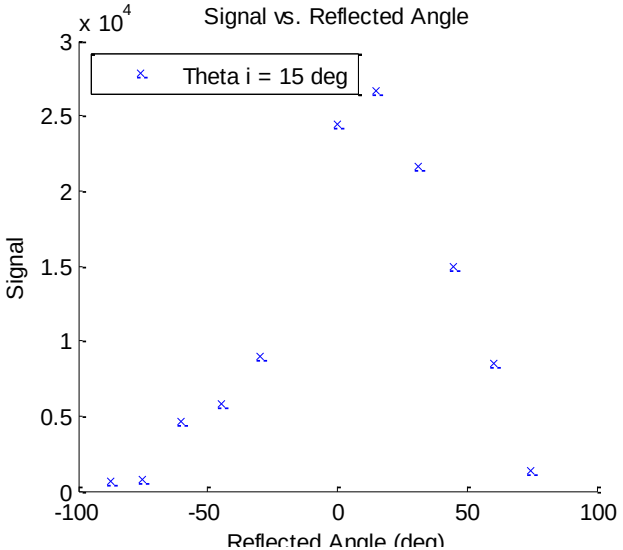

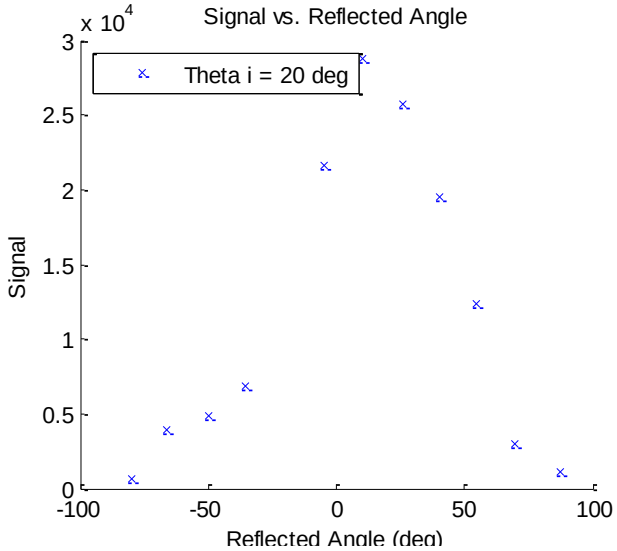

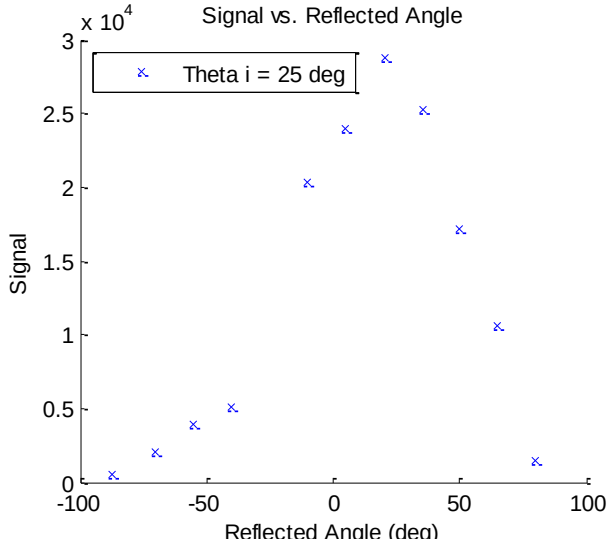

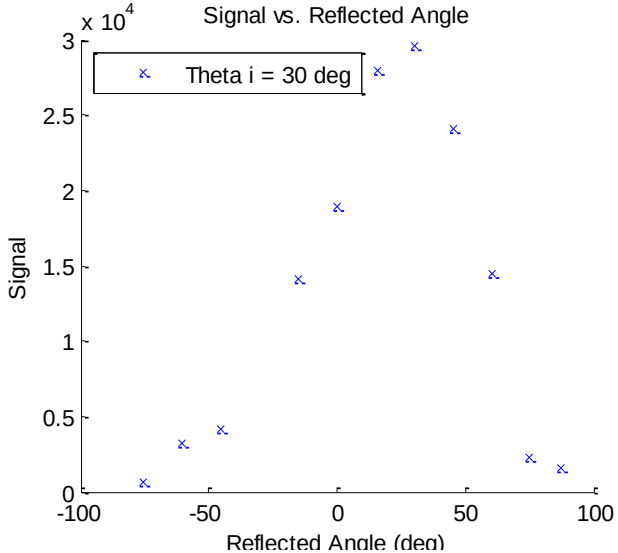

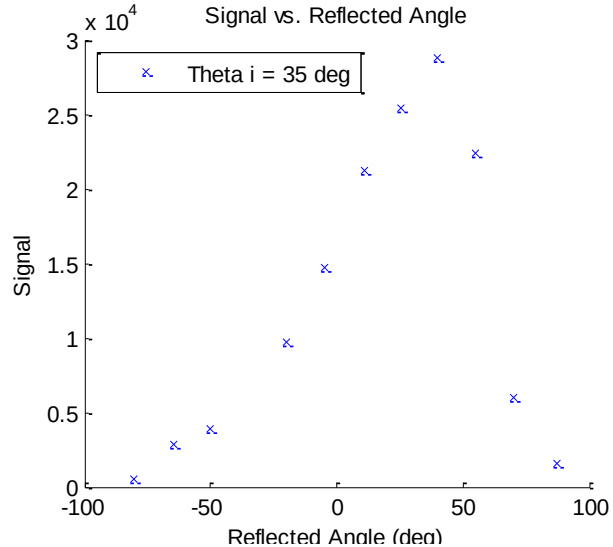

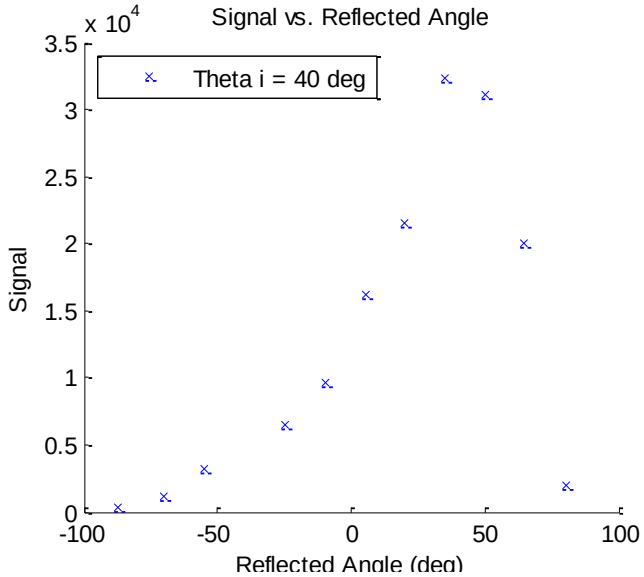

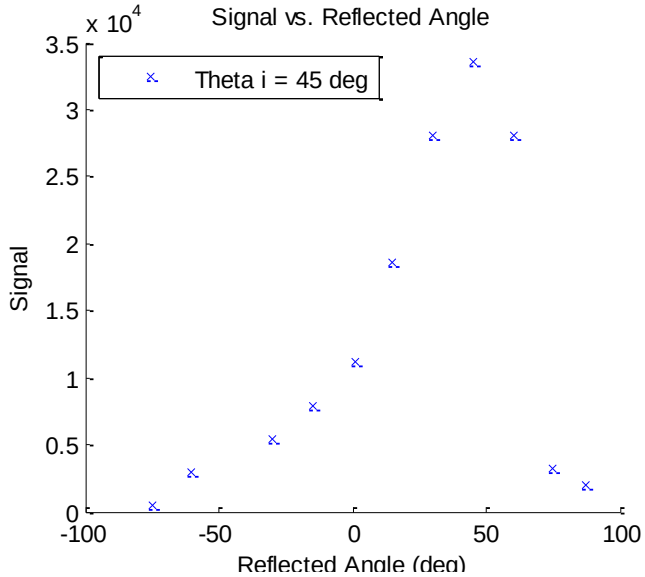

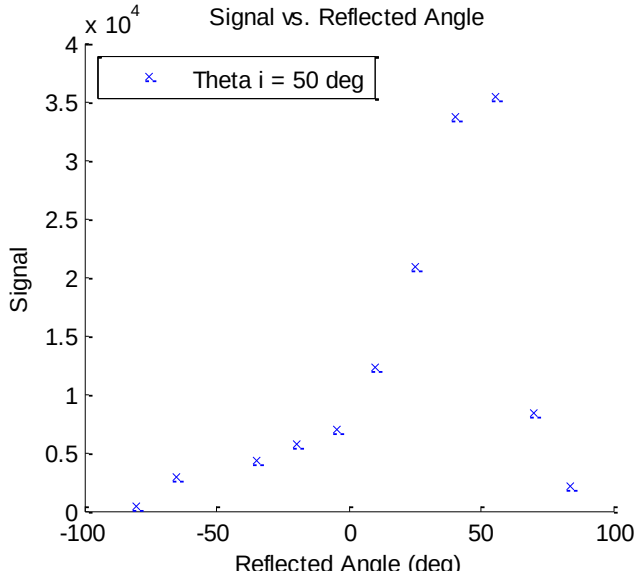

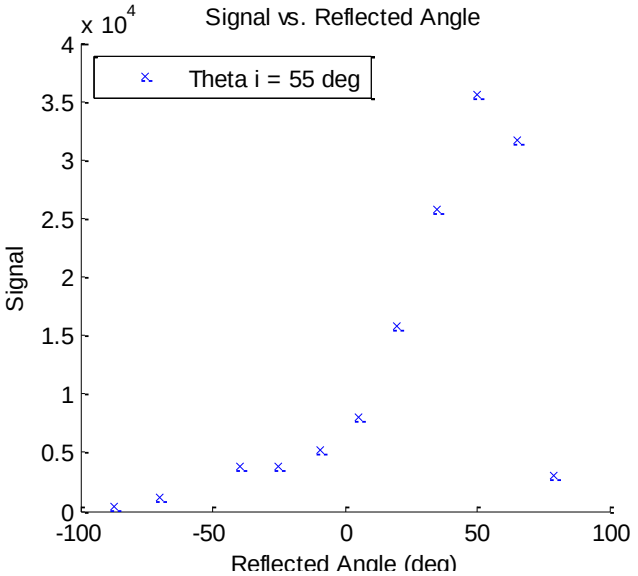

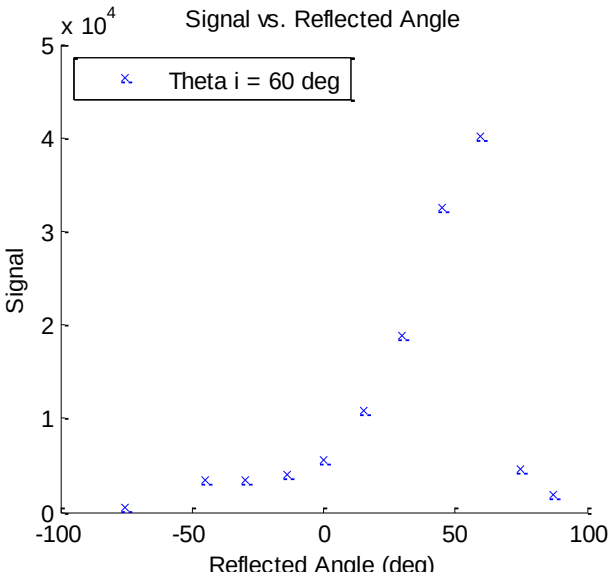

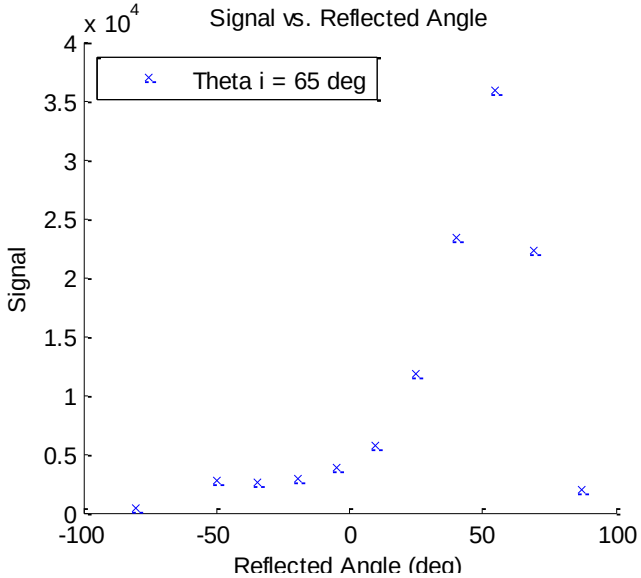

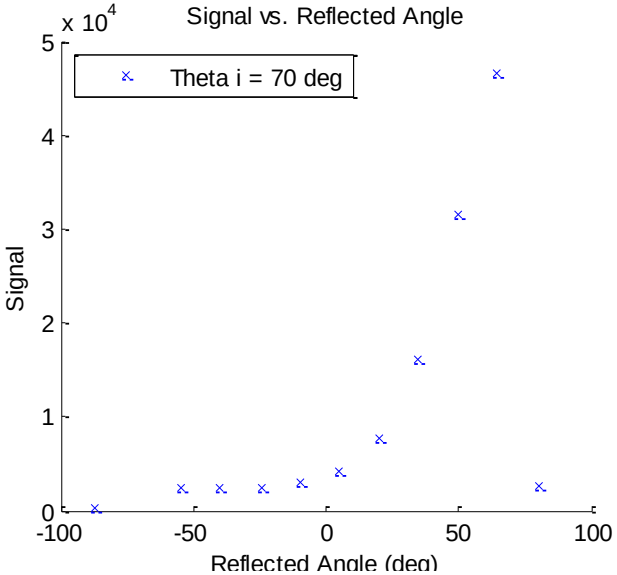

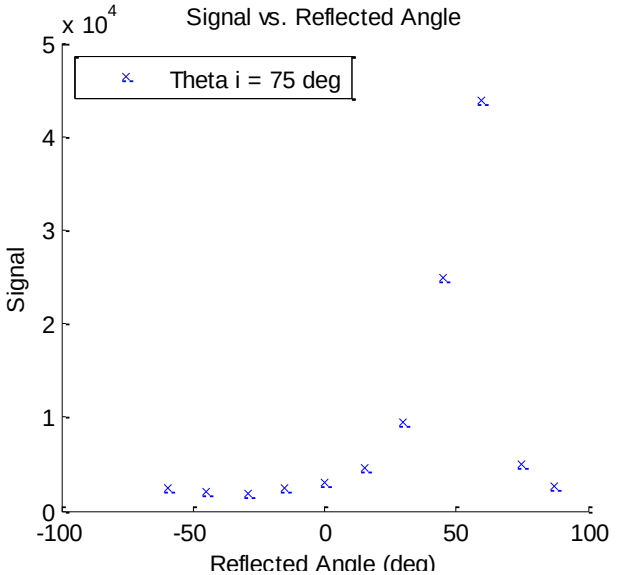

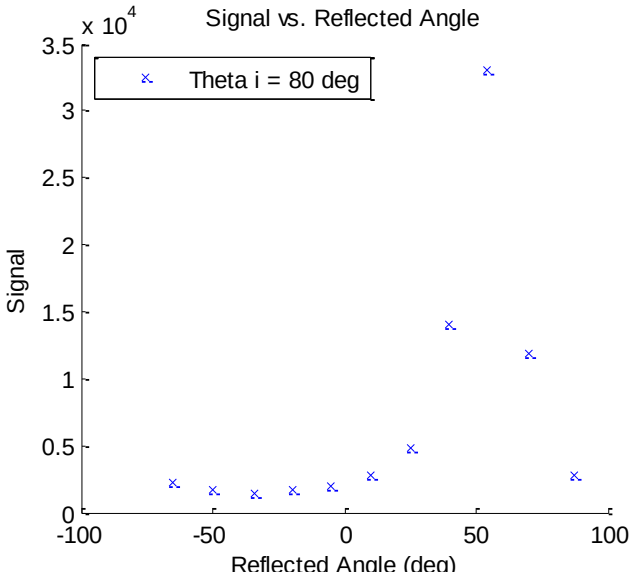

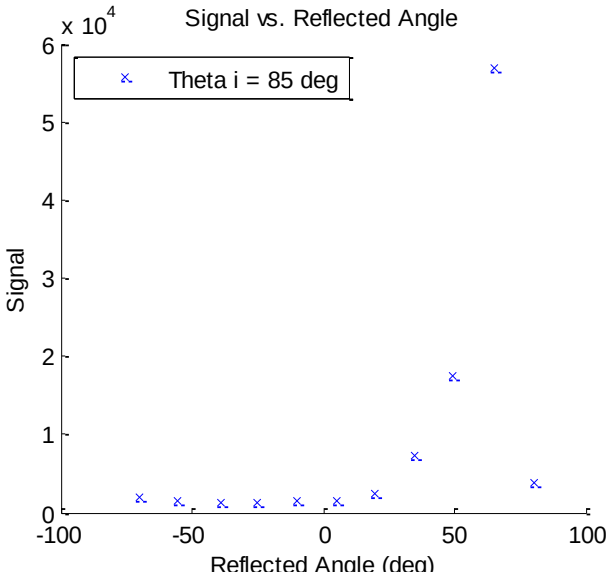

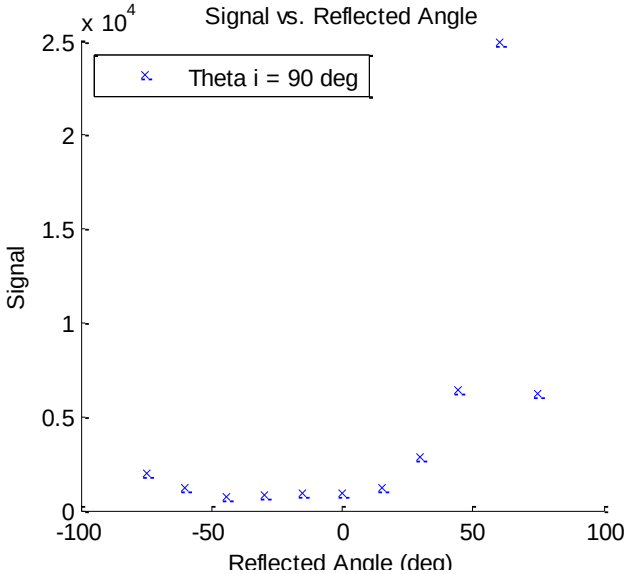

Appendix E – L3 / Tinsley Mirror Specifications

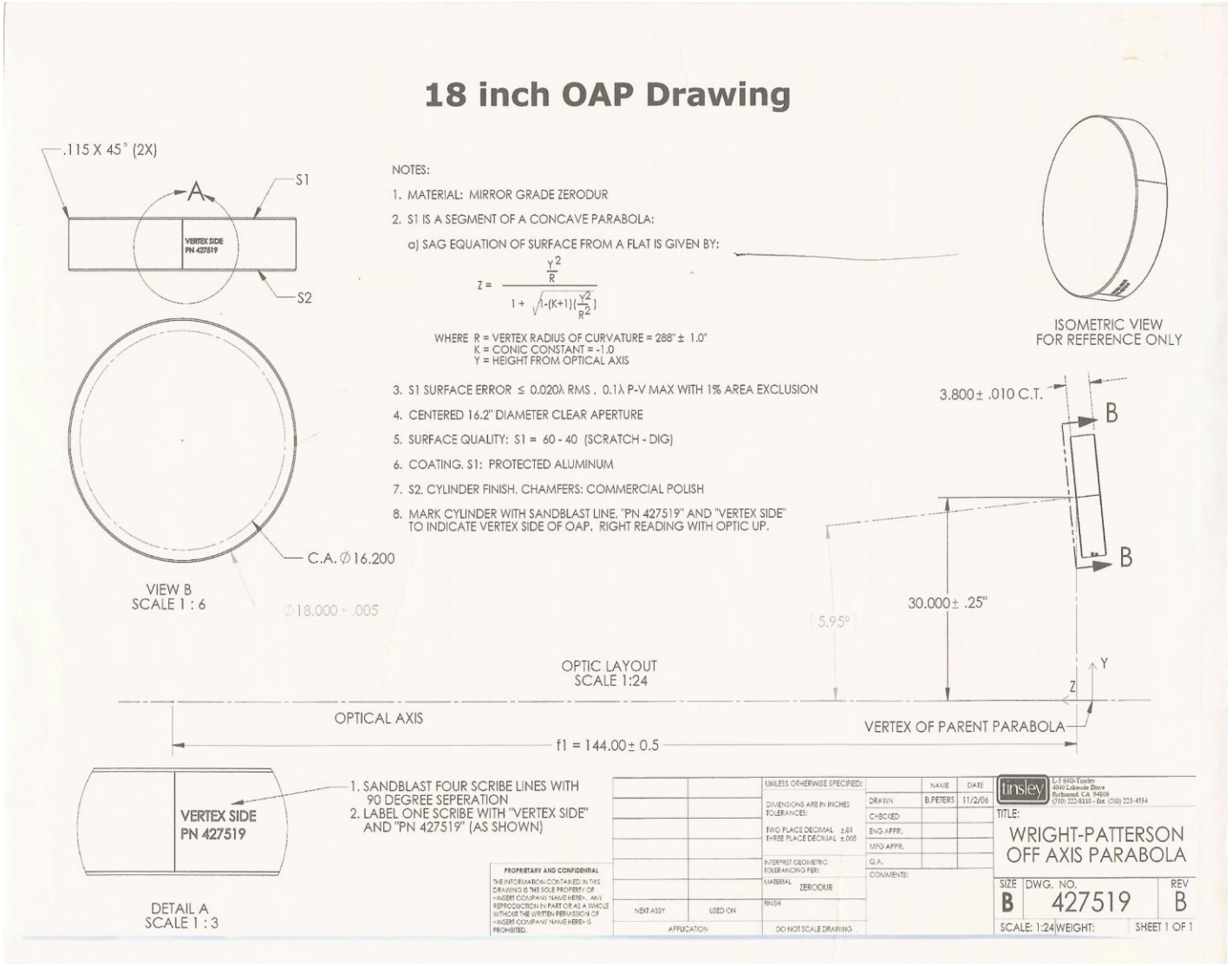

EMF Corp.
239 Cherry St. Ithaca, NY 14850
Phone 800.456.7070, Fax 800.456.3227

Reflectance Spectra

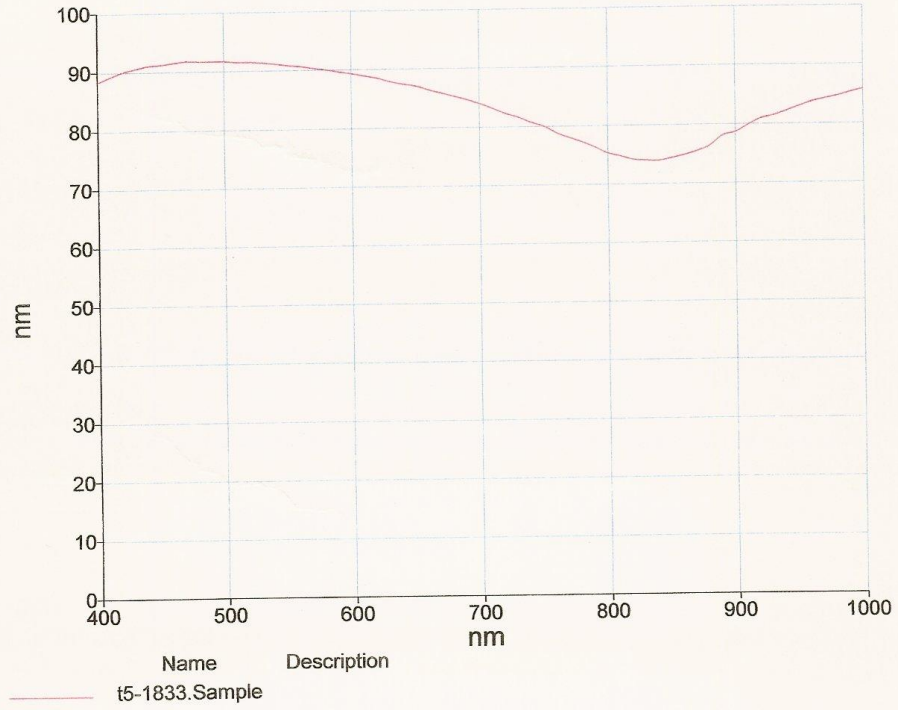

T5-1833 R(Avg) = 85.10 % from 400-1000nm

18 inch OAP Summary

Requirements	Actual	Pass/Fail
Mechanical Requirements		
Outer Diameter: 18.000" ± .005"	17.9995	Pass
Center Thickness: 3.800" ± .010"	3.8098	Pass
Chamfer S1 (Face Width): .115" ± .005"	.115	Pass
Chamfer S2 (Face Width): .115" ± .005"	.115	Pass
Optical Requirements		
Surface error Figure < .02 waves rms	.013 waves	Pass
Surface Irregularity < .10 waves PV with 1% exclusion	.074 waves	Pass
Parent Vertex Radius: 288" ± 1" Conic: -1.00 (no tolerance) Off-Axis Distance: 30" ± .25"	287.8* -1.00 (not varied) 29.997**	Pass Pass Pass
Surface Roughness < 20 Angstroms	15.42A	Pass
Surface Quality 60/40	<60/40	Pass

L3 communications
SSG-Tinsley

* Based on estimated accuracy of profilometer radius fit
** Based on estimated accuracy of profilometer off-axis distance fit

Final Inspection Map

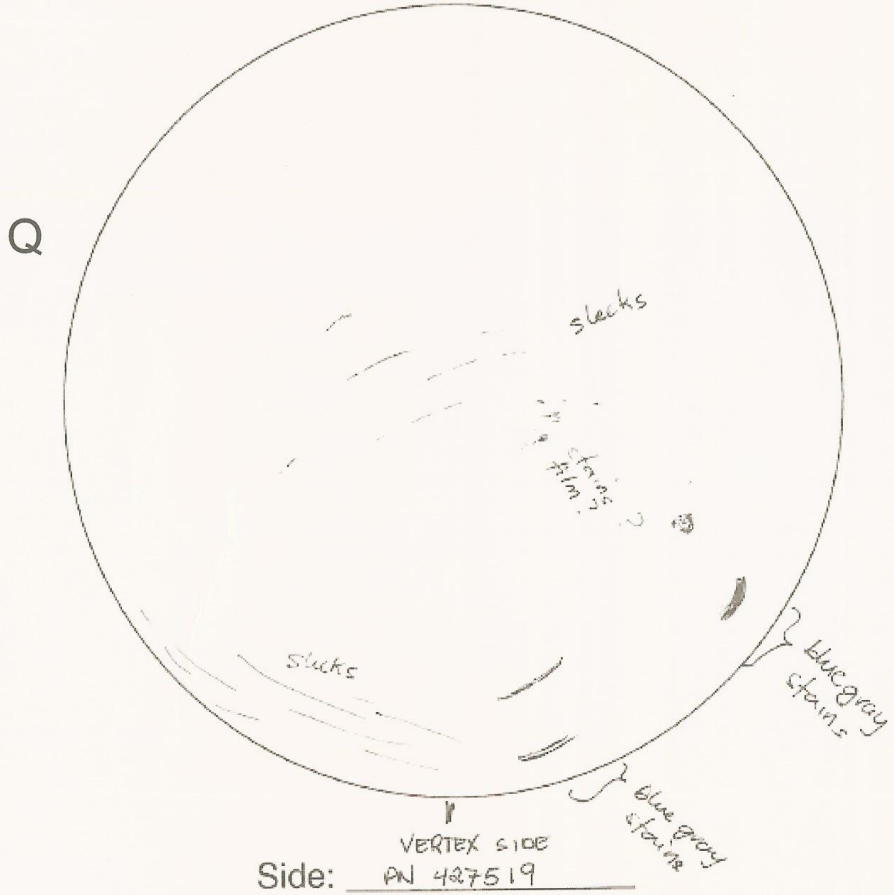

Side: PN 427519

L3 communications
SSG-Tinsley

Test Error Budget

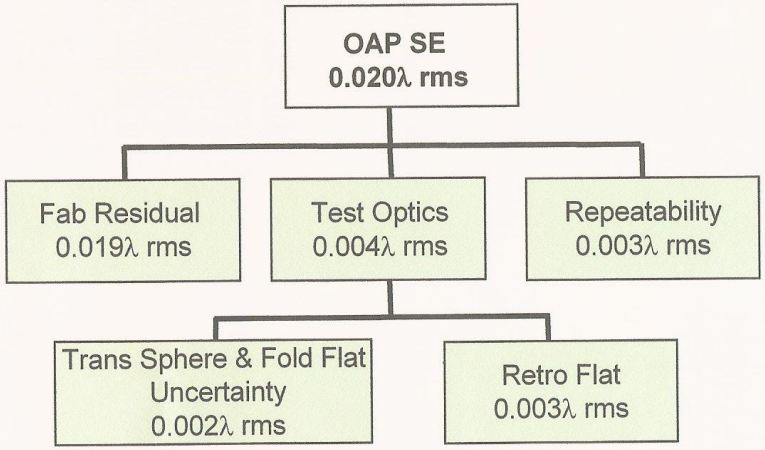

Actual fab residual (as measured) .012λ rms.

Predicted total error (rss fab residual, test optics, and repeatability) 0.013λ rms against 0.020λ rms requirement

**Test optics on slides 12 & 13

L3 communications
SSG-Tinsley

Clear Aperture 16.2" Diameter, Coated

```
file : final_a.ca

units: x = in
       y = in
       z = wv (hene)
xspac: 0.039
yspac: 0.039
ngx  : 511
ngy  : 511
gxcen: 0
gycen: 0

z ptv: 0.2178
z rms: 0.0124

x-apr: 16.15
y-apr: 16.15

z min:-0.07832
  @ (294, 55)
z max: 0.1395
  @ (281, 462)
z avg: 4.878e-005

npnts: 135509/261121

ix   : 269
iy   : 256
xpos : 0.5070
ypos : 0.0000
r    : 0.5070
theta: 0.0000
zval : -0.00579

color: jet
```

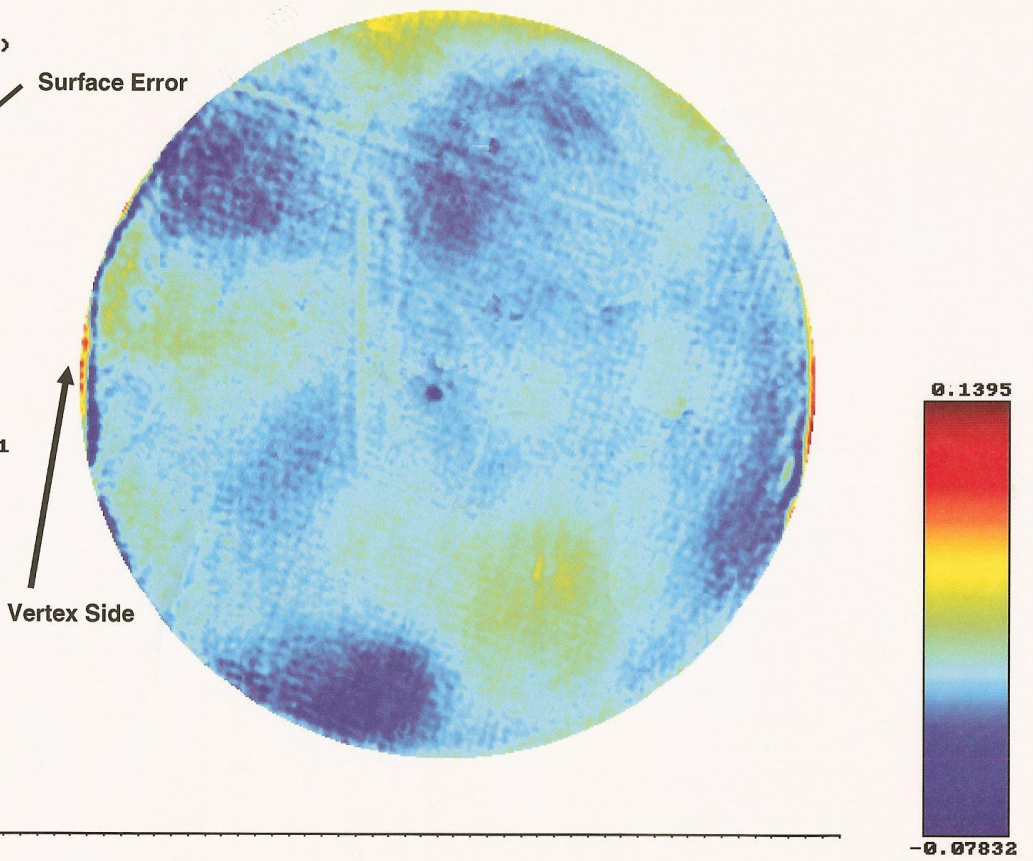

L3 communications
SSG-Tinsley

7

Clear Aperture 16.2" Diameter, 1 % Exclusion, Coated

```
file : final_a.99

units: x = in
       y = in
       z = wv (hene)
xspac: 0.039
yspac: 0.039
ngx  : 511
ngy  : 511
gxcen: 0
gycen: 0

z ptv: 0.07424
z rms: 0.01108

x-apr: 16.11
y-apr: 15.99

z min: 0
  @ (251, 55)
z max: 0.07424
  @ (53, 269)
z avg: 0.0368

npnts: 134156/261121

ix   : 256
iy   : 256
xpos : 0.0000
ypos : 0.0000
r    : 0.0000
theta: 0.0000
zval : 0.0256

color: jet
```

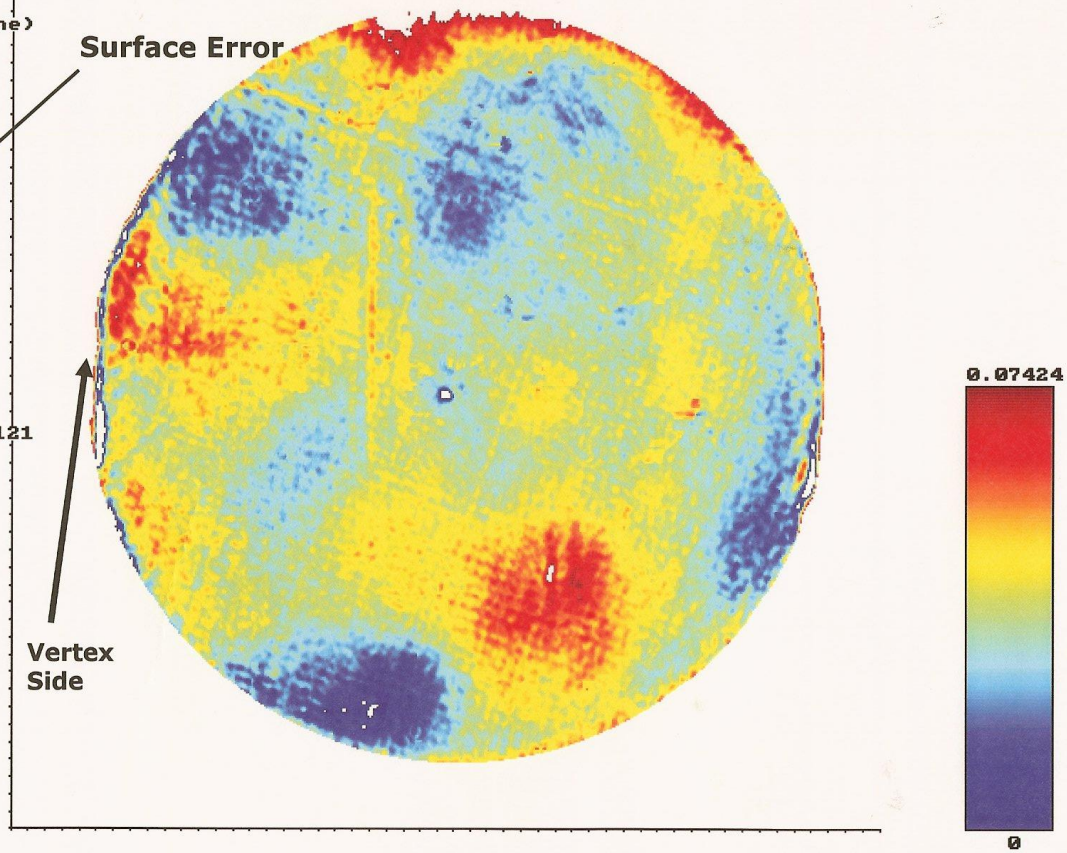

L3 communications
SSG-Tinsley

Clear Aperture 16.2” Diameter, Pre-coat

```
file : 0417_f.ca

units: x = in
       y = in
       z = wv (hene)
xspac: 0.039
yspac: 0.039
ngx  : 511
ngy  : 511
gxcen: 0
gycen: 0

z ptv: 0.2078
z rms: 0.01204

x-apr: 16.15
y-apr: 16.15

z min:-0.07211
  @ (309, 453)
z max: 0.1357
  @ (277, 462)
z avg:-1.44e-005

npnts: 135505/261121

ix   : 256
iy   : 256
xpos : 0.0000
ypos : 0.0000
r    : 0.0000
theta: 0.0000
zval : -0.00893

color: jet
```

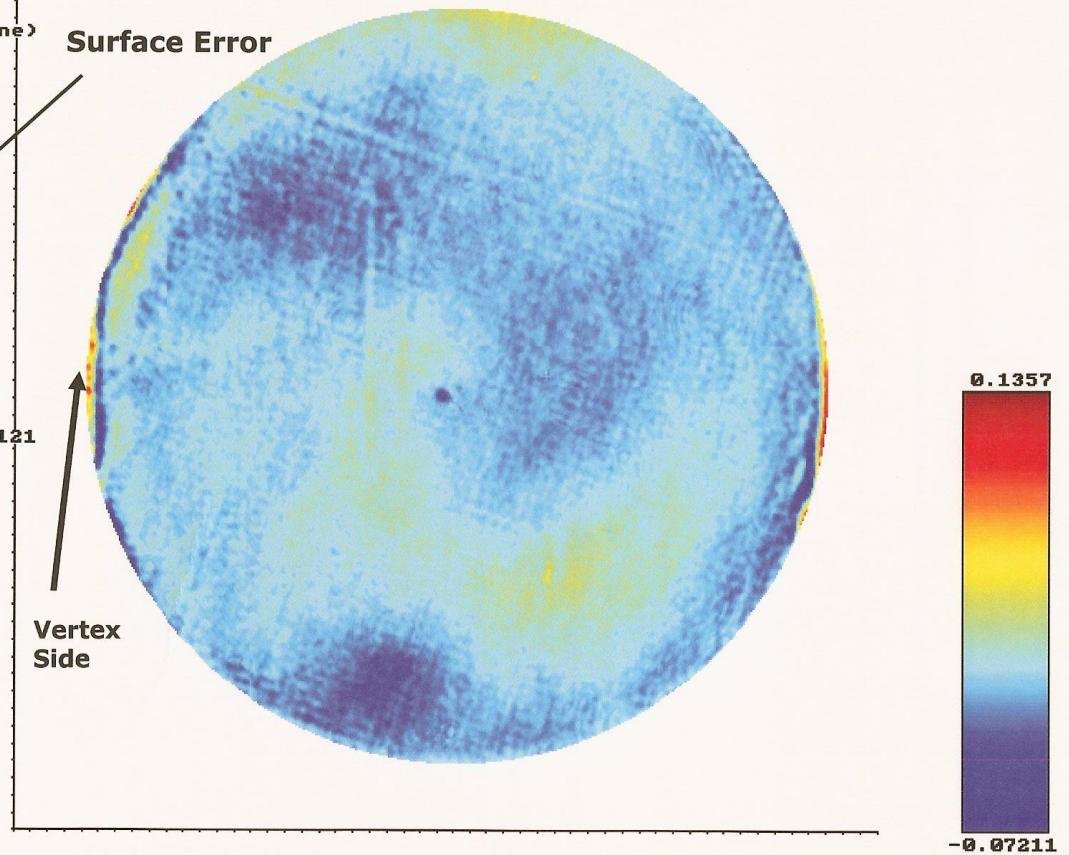

L3 communications
SSG-Tinsley

Clear Aperture 16.2” Diameter, 1 % Exclusion, Pre-coat

```
file : 0417_f.99

units: x = in
       y = in
       z = wv (hene)
xspac: 0.039
yspac: 0.039
ngx  : 511
ngy  : 511
gxcen: 0
gycen: 0

z ptv: 0.06766
z rms: 0.01071

x-apr: 16.15
y-apr: 16.03

z min: 0
  @ (211, 56)
z max: 0.06766
  @ (49, 265)
z avg: 0.03363

npnts: 134156/261121

ix   : 511
iy   : 168
xpos : 9.9450
ypos :-3.4320
r    : 10.5205
theta: 340.9605
zval : no data

color: jet
```

Surface Error

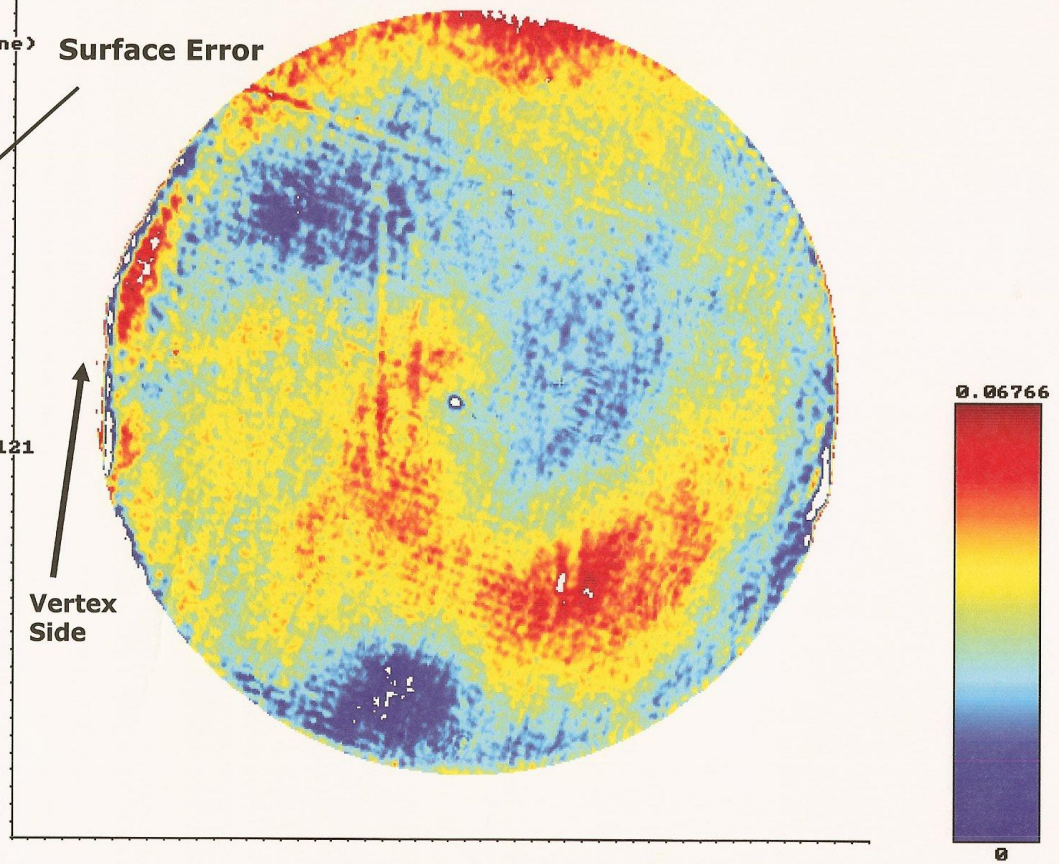

Vertex Side

L3 communications
SSG-Tinsley

10

Characteristic OAP Surface Roughness

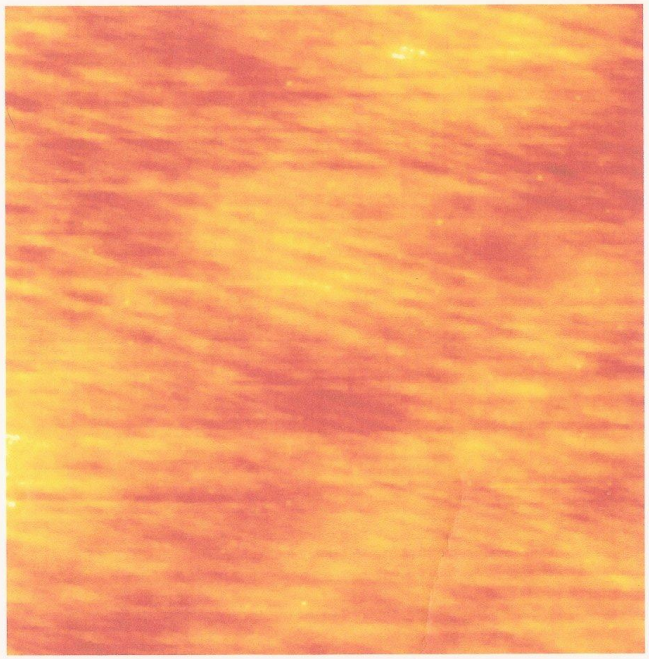

PV: 130.48 waves

RMS: 16.66 waves

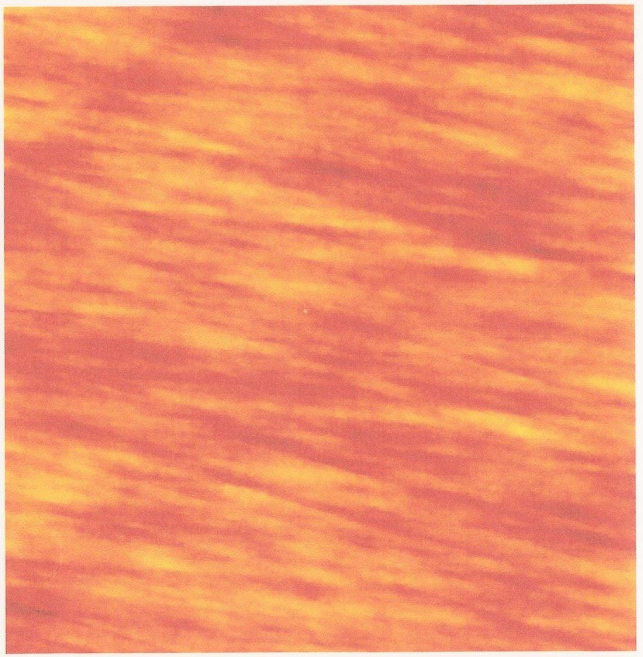

PV: 120.89 waves

RMS: 13.89 waves

L3 communications
SSG-Tinsley

11

Transmission Sphere and Fold Flat Cavity

```
file : 0417cav.ca

units: x = in
       y = in
       z = wv (hene)
xspac: 0.039
yspac: 0.039
ngx  : 511
ngy  : 511
gxcen: 0
gycen: 0

z ptv: 0.04561
z rms: 0.005968

x-apr: 16.15
y-apr: 16.15

z min:-0.02232
  @ (241, 207)
z max: 0.02329
  @ (267, 317)
z avg:-9.334e-006

npnts: 135509/261121

ix   : 256
iy   : 256
xpos : 0.0000
ypos : 0.0000
r    : 0.0000
theta: 0.0000
zval : 0.0025

color: jet
```

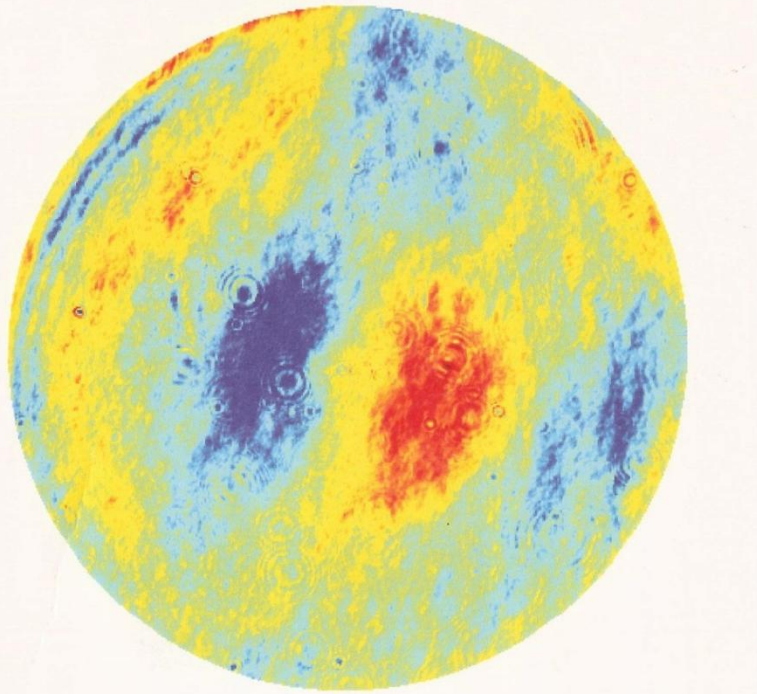

communications
SSG-Tinsley

12

Retro Flat

```
file : zernfit.res

units: x = in
       y = in
       z = wv (hene)
xspac: 0.01702
yspac: 0.01702
ngx  : 1024
ngy  : 1024
gxcen: 0.2337
gycen: 0.3363


z ptv: 0.04597
z rms: 0.002438


x-apr: 16.18
y-apr: 16.18


z min:-0.02306
  @ (308, 685)
z max: 0.02291
  @ (896, 557)
z avg: 3.92e-007

npnts: 711670/1048576


ix   : 513
iy   : 513
xpos : 0.2422
ypos : 0.3448
r    : 0.4213
theta: 54.9186
zval : 0.00396

color: jet
```

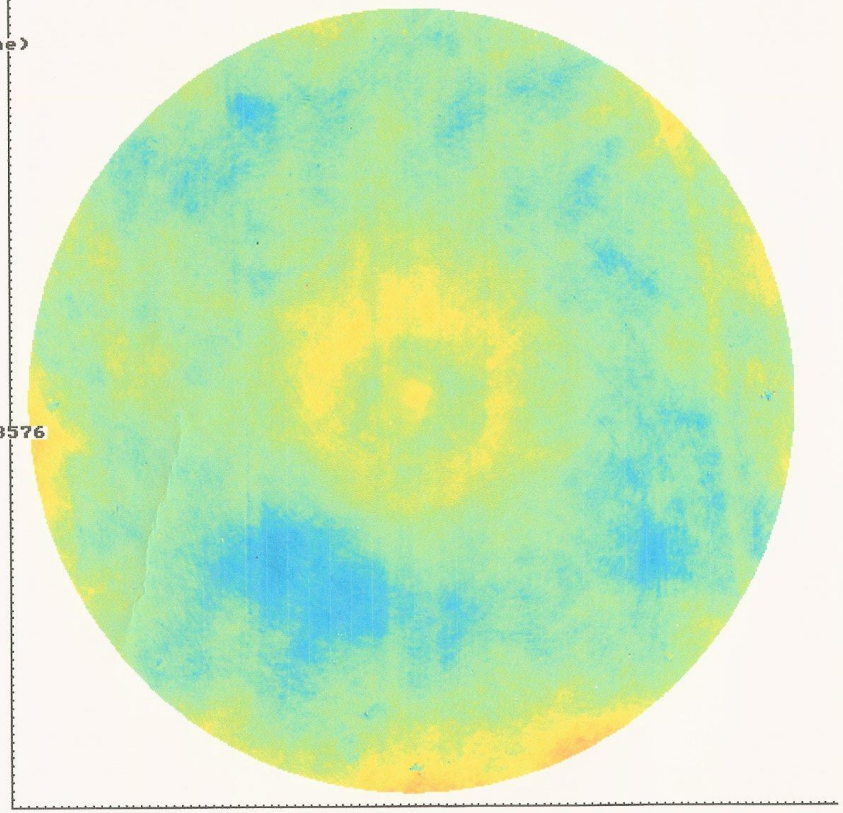

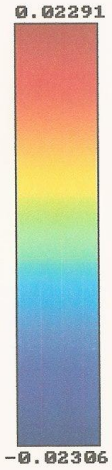

L3 communications
SSG-Tinsley

Bibliography

Bortle, J. (2006). *A Measurement and Prediction-Based Validation of the AFIT Large Commercial Aircraft Infrared Trend Analysis Tool.* Master's thesis, Air Force Institute of Technology(AETC), Graduate School of Management and Engineering, Department of Physics, Wright Patterson AFB.

Dereniak, E. L. (1996). *Infrared Detectors and Systems.* Wiley Interscience.

Harkiss, S. I. (2007). A Study of Bi-Directional Reflectance Distribution Functions and Their Effect on Infrared Signature Models. Dayton.

Marschner, S. R. (2000). Image Based BRDF Measurements. *Applied Optics , 39* (16).

Marschner, S. R. (1999). Image-based BRDF measurement including. *Eurographics Rendering Workshop.*

Mukaigawa, Y., Sumino, K., & Yagi, Y. (2007). High-Speed Measurement of BRDF using an Ellipsoidal Mirror and a Projector.

Nicodemus, F. E. (1977). *Geometrical Considerations and Nomenclature for Reflectance.* Washington: National Bureau of Standards.

Robertson, M. A. (1999). DYNAMIC RANGE IMPROVEMENT THROUGH MULTIPLE EXPOSURES. *International Conference on Image Processing* (pp. 159-163). IEEE.

Schirmacher, H., Heidrich, W., Rubick, M., Schiron, D., & Seidel, H.-P. (1999). Image-Based BRDF Reconstruction. *In Proceedings of the 4th Vision, Modeling, and Visualization Conference*, (pp. 285-292).

Strob, K., Sepp, W., Fuchs, S., Paredes, C., & Arbeter, K. (2007, April 13). *Camera Calibration Toolbox for Matlab*. Retrieved February 1, 2008, from Caltech: http://www.vision.caltech.edu/bouguetj/calib_doc/

REPORT DOCUMENTATION PAGE

Form Approved
OMB No. 0704-0188

PLEASE DO NOT RETURN YOUR FORM TO THE ABOVE ORGANIZATION.

1. REPORT DATE *(DD-MM-YYYY)*	2. REPORT TYPE	3. DATES COVERED *(From - To)*
27-03-2008	Master's Thesis	September 2007 - March 2008

4. TITLE AND SUBTITLE

An Image Based Bidirectional Reflectivity Distribution Function Experiment

5a. CONTRACT NUMBER

Proposal 2007-162, JON 08-117

5b. GRANT NUMBER

5c. PROGRAM ELEMENT NUMBER

6. AUTHOR(S)

Hagg, Michael T., Captain, USAF

5d. PROJECT NUMBER

5e. TASK NUMBER

5f. WORK UNIT NUMBER

7. PERFORMING ORGANIZATION NAME(S) AND ADDRESS(ES)

Air Force Institute of Technology
Graduate School of Engineering and Management (AFIT/EN)
2950 Hobson Way, WPAFB OH 45433-7765

8. PERFORMING ORGANIZATION REPORT NUMBER

AFIT/GEO/ENP/08-M03

9. SPONSORING/MONITORING AGENCY NAME(S) AND ADDRESS(ES)

AFRL/RYS
Attn: Mr. Jeffery Burks
2591 K Street
WPAFB OH 45433-7765

10. SPONSOR/MONITOR'S ACRONYM(S)

AFRL/RYS

11. SPONSOR/MONITOR'S REPORT NUMBER(S)

12. DISTRIBUTION/AVAILABILITY STATEMENT

APPROVED FOR PUBLIC RELEASE; DISTRIBUTION UNLIMITED

13. SUPPLEMENTARY NOTES

14. ABSTRACT

This experiment is a proof of concept type experiment providing initial setup and discovery of pitfalls that need to be overcome for AFIT to set-up an image based BRDF acquisition tool. Custom fabricated parts including a robust camera rotation mount and large scale mirror solutions are discussed.

Image data extraction including geometric pixel to surface area correlation and a discussion of radiometric quantities that need to be well documented to extract BRDF.

15. SUBJECT TERMS

Reflectivity, Distribution Function, Images, Camera Mounts, Mirrors

16. SECURITY CLASSIFICATION OF:			17. LIMITATION OF ABSTRACT	18. NUMBER OF PAGES	19a. NAME OF RESPONSIBLE PERSON
a. REPORT	b. ABSTRACT	c. THIS PAGE			Michael Marciniak, PhD
U	U	U	UU	80	19b. TELEPHONE NUMBER *(Include area code)* (937) 255-3636 x 4529 michael.marciniak@afit.edu

Reset

Standard Form 298 (Rev. 8/98)
Prescribed by ANSI Std. Z39.18